Universal Approach for Quantum Interfaces with Atomic Arrays

Yakov Solomons, Roni Ben-Maimon, and Ephraim Shahmoon*
Department of Chemical & Biological Physics, Weizmann Institute of Science, 7610001 Rehovot, Israel

(Received 9 February 2023; revised 2 December 2023; accepted 2 April 2024; published 7 May 2024)

We develop a general framework for the analysis of two-sided quantum interfaces, composed of collections of atoms interacting with paraxial light. Accounting for photon-mediated dipole-dipole interactions, our approach is based on the mapping of collective atom-photon interfaces onto a generic one-dimensional model of light scattering, characterized by a reflectivity parameter r_0. This entails two key practical advantages: (i) the efficiency of the quantum interface in performing various quantum tasks, such as quantum memory or entanglement generation, is universally given by r_0 and is hence reduced to a measurement or classical calculation of a reflectivity; (ii) the efficiency can be greatly enhanced by a properly designed photon mode that spatially matches a collective-dipole eigenmode of the atoms. We demonstrate our approach for realistic cases of finite-size atomic arrays, partially filled arrays, and circular arrays. This provides a unified approach for treating collective light-matter coupling in various platforms, such as optical lattices and optical tweezers.

DOI: 10.1103/PRXQuantum.5.020329

I. INTRODUCTION

Quantum optical platforms, based on the manipulation of atoms and photons, play an essential role in the exploration of quantum science and technology. Of crucial importance is the ability to establish an interface between photons and atoms. Such an interface allows one to benefit from the low-loss propagation of photons combined with the quantum coherence or nonlinearity of atoms, with applications ranging from quantum memories and information to many-body physics [1,2]. To this end, a quantum interface is required to couple a certain target photon mode that one excites and detects to a relevant spatially matched atomic degree of freedom. In turn, the efficiency of the interface is characterized by the ratio between the emission rate of the atomic degree of freedom to the target mode and that to the rest of the undesired modes. This ratio depends on the specific realization: for an ensemble of atoms trapped in free space [3–13] or along a waveguide [14,15], it is typically given by the so-called optical depth (OD), whereas for atoms trapped inside a cavity, this ratio is often identical to the cooperativity parameter [16,20–24].

Recently, spatially ordered arrays of trapped atoms, as can be realized in an optical lattice [25,26], have emerged as a novel quantum light-matter interface [27–49]. For arrays with near-wavelength lattice spacing, the combination of spatial order with the collective response of the atoms to light considerably reduces the scattering into unwanted directions. This results in strong and directional light-matter coupling between a propagating, target photon mode and a spatially matched collective dipole of the atoms. In two-dimensional (2D) arrays, the strength of the coupling is evident and is characterized by the high reflectivity of the target mode scattered off the array [28–30]. Moreover, the reflectivity seems to appear in relation to efficiencies of various quantum applications that were subsequently proposed, from quantum entanglement generation and information with photons [50–55] to optomechanics [36,37] and quantum memories [27,31]. However, no clear relation or framework that underscores the general role of array reflectivity in such light-matter applications had been established thus far.

In this work, we provide a general approach for the analysis of two-sided quantum interfaces and apply it to various realistic atom-array problems. We begin by finding general conditions under which collective atom-photon interfaces can be mapped to a generic one-dimensional (1D) model of scattering characterized by a reflectivity. This mapping entails two important consequences: (i) the efficiency of the quantum interface in performing various quantum tasks is characterized by a measurement or a simple classical calculation of a reflectivity; (ii) we show how the reflectivity, and hence the efficiency, can be greatly enhanced by a properly designed photon mode that spatially matches the collective eigenmodes of the array structure.

*Corresponding author: ephraim.shahmoon@weizmann.ac.il

Published by the American Physical Society under the terms of the Creative Commons Attribution 4.0 International license. Further distribution of this work must maintain attribution to the author(s) and the published article's title, journal citation, and DOI.

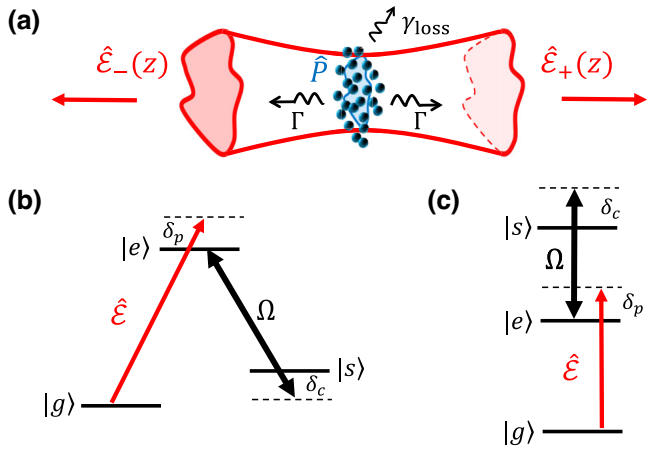

FIG. 1. Generic 1D model of a two-sided light-matter interface [Eq. (1)] onto which various systems are mapped. (a) A collective dipole $\hat{P}$ of the atomic system is coupled to a spatially matched, target photon mode $\hat{\mathcal{E}}$ at an emission rate Γ, while scattering to other modes (loss) at rate γ_{loss}. The atom-photon coupling is taken to be symmetric on both sides [Eq. (4)]. (b) Level structure of the atoms in the three-level variant of the model, with a tunable coupling field $\Omega(t)$ [Eq. (6)]. (c) Ladder-configuration version of three-level atom scheme.

A. Outline and scope

We begin with a brief account of the scope and results.

1. 1D model of a quantum interface: Reflectivity as a figure of merit (Sec. II)

We introduce a minimal 1D model for a two-sided atom-photon interface, depicted in Fig. 1: A collective mode of atomic dipoles $\hat{P}$ is coupled to a one-dimensionally-propagating "target" photon mode $\hat{\mathcal{E}}$, while also scattering to other modes considered as a loss. Denoting the ratio of these couplings by the cooperativity $C = \Gamma/\gamma_{\text{loss}}$, it is found that the on-resonance reflectivity of the target mode, given by $r_0 = C/(C+1)$, fully characterizes atom-photon coupling. In particular, r_0 is equal to the efficiency of energy conversion between the dipole $\hat{P}$ and the target mode $\hat{\mathcal{E}}$ and hence emerges as a universal figure of merit of quantum tasks. This is demonstrated for efficiencies of quantum memory and entanglement generation, analyzed for corresponding linear and nonlinear variants of the 1D model.

2. Mapping to the 1D model (Secs. III and VII)

For a given atom-photon system, the first challenge is to identify the mapping to the two-sided 1D model. We consider a general collection of atoms interacting with a paraxial target photon mode in free space, accounting for collective effects established by induced dipole-dipole interactions between the atoms. Beginning with a collection of atoms arranged on a plane, we find in Sec. III that the mapping is possible if the transverse profile of the target mode $\hat{\mathcal{E}}$ spatially matches an eigenmode $\hat{P}$ of the dipole-dipole interaction kernel, whose eigenvalue we denote by D_0 [Fig. 1(a)]. While $\hat{P}$ can decay to both the target mode $\hat{\mathcal{E}}$ and to other photon modes at total rate $\Gamma_0 = 2\text{Re}[D_0]$, we independently find an expression for its rate of coupling to the target mode $\Gamma \leq \Gamma_0$, yielding the mapping parameters Γ and $\gamma_{\text{loss}} = \Gamma_0 - \Gamma$ (in the absence of other single-atom losses). In Sec. VII we extend the analysis to multiple layers of such planar atomic ensembles, finding that when the distance between the layers is an integer multiple of half of the resonant wavelength (Bragg condition), then the mapping to the two-sided 1D model is still possible, with the rates Γ_0 and Γ both now multiplied by the number of layers.

3. Examples (Secs. IV–VII)

We apply our approach for the description and design of realistic atom-array interfaces:

(i) Two-dimensional and three-dimensional (3D) lattice arrays (Secs. IV and VII). We derive useful analytical results for typical cases of ordered arrays considering their finite size and position disorder, as summarized in Tables I and II. We establish the mapping to the 1D model, showing that a target photon mode in a typical Gaussian-beam shape matches an approximate eigenmode of the dipole-dipole interaction, whereas any deviations due to imperfections and finite-size effects are accounted for by the loss parameter γ_{loss}. Analytical results for r_0 derived from the mapping are shown to agree with numerical results for both the reflectivity and the efficiency of a quantum memory protocol.

(ii) Partially filled arrays (Sec. V). Considering a 2D ordered array (lattice) with static disorder in the form of a finite filling fraction, we show how the reflectivity can be greatly enhanced if we go beyond the typical case of a Gaussian-beam target mode. Remarkably, by choosing a target mode that matches a dipole eigenmode, we obtain efficiencies r_0 of 0.99 and 0.94 for filling fractions as low as 85% and 70%, respectively, instead of much lower efficiencies with a Gaussian-beam target mode. The analytical results agree with the numerical ones, showing that the mapping is valid and hence that the enhancement of r_0 implies enhanced efficiencies of quantum tasks.

(iii) Circular arrays (Sec. VI). As another deviation from the translation-invariant case of a lattice, we consider a circular array. We demonstrate different choices of target modes corresponding to different dipole eigenvalues of the circular structure, again finding good agreement between r_0 predicted by our theory and numerical scattering calculations.

II. GENERIC 1D MODEL: REFLECTIVITY

We begin by introducing the 1D scattering model of a two-sided quantum interface onto which collective atom-photon systems are mapped within our approach.

A. The model

We consider a paraxial mode of light with some finite mode area, e.g., a Gaussian beam within its Rayleigh range, propagating along the z direction and described by the 1D field operator $\hat{\mathcal{E}}(z,t)$, with $[\hat{\mathcal{E}}(z),\hat{\mathcal{E}}^\dagger(z')] \propto \delta(z-z')$. This "target mode" interacts with a collection of two-level atoms and couples to a spatially matched collective mode of their atomic dipoles, described by the operator $\hat{P}$ [Fig. 1(a)]. However, since the "collective dipole" $\hat{P}$ comprises discrete atoms, it may, in general, also scatter to other undesired photonic modes in different directions. A simple model that captures this scenario is given by

$$\frac{d\hat{P}}{dt} = \left[i(\delta_p-\Delta) - \frac{\Gamma+\gamma_{\rm loss}}{2}\right]\hat{P} + i\sqrt{\Gamma}\hat{\mathcal{E}}_0(0,t) + \hat{F}(t),$$
$$\hat{\mathcal{E}}(z) = \hat{\mathcal{E}}_0(z) + i\sqrt{\Gamma}\hat{P}. \tag{1}$$

These Heisenberg-picture equations describe a 1D problem of the target mode $\hat{\mathcal{E}}(z)$ scattered off the collective dipole $\hat{P}$. Here, Γ is the emission rate of the atomic dipole to the target-mode 1D continuum, with an input quantum field satisfying $[\hat{\mathcal{E}}_0(0,t),\hat{\mathcal{E}}_0^\dagger(0,t')] = \delta(t-t')$, whereas $\gamma_{\rm loss}$ is the emission rate to the undesired modes with corresponding quantum vacuum noise $\langle\hat{F}(t)\hat{F}^\dagger(t')\rangle = \gamma_{\rm loss}\delta(t-t')$. $\delta_p = \omega_p - \omega_a$ is the detuning between the central frequency of the target mode (ω_p) and that of the "bare" two-level atom transition (ω_a), whereas Δ is a possible collective shift of the collective atomic dipole. Assuming that the number of atomic excitations is much lower than the number of constituent two-level atoms that comprise the collective dipole, we begin by considering the operator $\hat{P}$ as a linearized bosoniclike mode (with $[\hat{P},\hat{P}^\dagger]=1$), while the inclusion of nonlinearities is discussed further below.

B. Cooperativity and coupling efficiency

We define the cooperativity C as the branching ratio between the emission to the desired target mode and that to undesired modes,

$$C = \frac{\Gamma}{\gamma_{\rm loss}}. \tag{2}$$

Quantum mechanically, this is a ratio of spontaneous emission rates, but it also has a clear classical meaning as the ratio of radiated energy or power. In Appendix A we illustrate this point in two ways. First, we consider an initially excited dipole $\hat{P}$ and calculate classically the fraction of energy radiated into the target mode, finding

$$r_0 \equiv \frac{C}{C+1}. \tag{3}$$

Second, we consider an input continuous wave (cw) illumination in the target mode and calculate the fraction of the power absorbed by the dipole $\hat{P}$ in the steady state. At resonance $\delta_p = \Delta$, we again obtain r_0 from Eq. (3). Therefore, r_0 describes the efficiency of light-matter coupling between the target mode and the atoms. It originates in the underlying classical linear optics problem and is determined by C. We discuss the relation of C and r_0 defined here to other definitions of cooperativity further below (see Sec. II E).

C. Reflectivity as an efficiency

The coupling efficiency from Eq. (3) can be physically interpreted as the reflectivity of the 1D scattering problem, a fact which can become practically useful as discussed further below. To show that r_0 is a reflectivity, we first note that the model from Eq. (1) pertains to a two-sided problem by identifying the field operator $\hat{\mathcal{E}}$ as the symmetric superposition of corresponding right–propagating and left-propagating components $\hat{\mathcal{E}}_\pm$, i.e., $\hat{\mathcal{E}}(z) = \frac{1}{\sqrt{2}}[\hat{\mathcal{E}}_+(z) + \hat{\mathcal{E}}_-(-z)]e^{-ik_p z}$ ($k_p \equiv \omega_p/c, z>0$); see Fig. 1(a). The input field in the equation for $\hat{P}$ is then $\hat{\mathcal{E}}_0(0) = \frac{1}{\sqrt{2}}[\hat{\mathcal{E}}_{0,+}(0) + \hat{\mathcal{E}}_{0,-}(0)]$, and the equation for the output field of each component is

$$\hat{\mathcal{E}}_\pm(z) = \hat{\mathcal{E}}_{0,\pm}(z) + i\sqrt{\frac{\Gamma}{2}}e^{\pm ik_p z}\hat{P}. \tag{4}$$

For classical cw light shined either from the right or from the left, we find the amplitude reflectivity as (see Appendix A)

$$r = -\frac{\Gamma}{\Gamma+\gamma_{\rm loss}+i2(\Delta-\delta_p)} \;\rightarrow\; r_0 = |r(\delta_p=\Delta)|. \tag{5}$$

We thus identify that the magnitude of this *field* reflectivity at resonance, r_0, is equal to the efficiency associated with *power* conversion from Eq. (3). For the intensity (power) reflectivity, we thus have $R = r_0^2$, which lends itself to an intuitive two-step picture of reflectivity: first, the photons of the target mode are absorbed by the atoms at efficiency r_0, as discussed in the previous subsection, and then they are emitted from the atoms to the target mode also at efficiency r_0, leading to $R = r_0^2$. While in a cw scenario this two-step process never really occurs at a certain timing, this simple picture is useful to understand the physics of the quantum memory discussed below.

D. Efficiency of quantum tasks

So far, we have seen that the linear reflectivity r_0 quantifies energy conversion between light and matter. Quantum mechanically, this amounts to the efficiency of converting atomic excitations to photons and vice versa. We therefore expect the reflectivity r_0 to also appear in efficiencies of quantum processes and tasks that rely on the coupling of atomic and photonic excitations. Intuitively, this should be the case as long as the system can be described by the 1D model, since r_0 is the sole parameter quantifying light-matter coupling. Namely, while different quantum processes and tasks may require corresponding variations to the 1D model as discussed below, these variations differ only in the atomic part, and not in their atom-photon coupling part, characterized by r_0.

We consider two types of quantum processes, linear and nonlinear. In the former, one is typically interested in faithfully transferring quantum properties, such as the quantum state or certain quantum correlations, of an atomic system to a photonic one or vice versa. This can be done either dissipatively or coherently, for purposes of, e.g., quantum memory or communication. Intuitively, since the essence of such a linear transformation amounts to the conversion of excitations between light and matter, we would expect that r_0 characterizes the efficiency of such tasks, as explained above. Mathematically, this is seen by the fact that the model (1) is essentially characterized by a single parameter, r_0 (equivalently C), which should characterize all the physics. In Sec. II D 1 below, we show that this is indeed the case for a typical quantum memory protocol.

In nonlinear processes, one typically exploits nonlinearities in the atomic system to generate quantum correlations between atomic excitations, which could also be translated to correlations between outgoing photons. The strength of the bare atomic nonlinearity is a parameter that may be independent of r_0. However, here as well we expect r_0 to appear in the efficiency of the generation of quantum correlations and their strength: To create atomic excitations in the first place, one typically shines light, so that r_0 would appear due to the conversion of the driving light to atomic excitations. Then, for the generation of correlated photons, correlated atomic excitations are converted back to light, hence again invoking r_0. We demonstrate this using a modification of the 1D model (1) that includes a nonlinearity, discussing two regimes: weak nonlinearity (Sec. II D 2) and blockade nonlinearity (Sec. II D 3).

1. Quantum memory efficiency

A relevant example of a linear quantum task is that of a quantum memory. Although the essence of the physics of excitation transfer in a quantum memory is captured by the model (1) as discussed above, the explicit memory protocol involves a modified atomic structure with a pair of stable levels. To this end, consider that the atomic system comprises three-level atoms, with a stable level $|s\rangle$ in addition to the ground state $|g\rangle$ and the excited state $|e\rangle$ [Fig. 1(b)]. Then there exists another relevant collective atomic operator, $\hat{S}$, which accounts for the coherence between the stable levels $|g\rangle$ and $|s\rangle$, and that is coupled to $\hat{P}$ (associated with the levels $|g\rangle$ and $|e\rangle$) via an external field Ω. Equation (1) is now modified to

$$\begin{aligned}\frac{d\hat{P}}{dt} &= \left[i(\delta_p-\Delta)-\frac{\Gamma+\gamma_{\rm loss}}{2}\right]\hat{P}+i\Omega\hat{S}\\ &\quad +i\sqrt{\Gamma}\hat{\mathcal{E}}_0(0,t)+\hat{F}(t),\\ \frac{d\hat{S}}{dt} &= i\delta_2\hat{S}+i\Omega^*\hat{P},\\ \hat{\mathcal{E}}(z) &= \hat{\mathcal{E}}_0(z)+i\sqrt{\Gamma}\hat{P},\end{aligned} \tag{6}$$

where $\delta_2=\delta_p-\delta_c$ is the combined detuning of the two-photon transition from $|g\rangle$ to $|s\rangle$ [Fig. 1(b)], and the emission rate to undesired modes $\gamma_{\rm loss}$ and the corresponding quantum vacuum noise $\hat{F}(t)$ may now include contributions from processes involving the third level.

The goal of a quantum memory is to coherently transfer the excitations and the quantum state of a pulse of the target mode $\hat{\mathcal{E}}$ into the stable atomic coherence $\hat{S}$. A second goal is to be able to retrieve these excitations and the quantum state from $\hat{S}$ back to the propagating mode of $\hat{\mathcal{E}}$. Within this process, the dipole $\hat{P}$ mediates the interaction between the field and the stable coherence $\hat{S}$, via the tunable coupling $\Omega(t)$. To see this, we adiabatically eliminate $\hat{P}$ from Eq. (6), obtaining an equation for $\hat{S}$ (see Appendix B)

$$\frac{d\hat{S}}{dt}=\left[i(\delta_2-\Delta_s)-\frac{\Gamma_S+\gamma_{\rm loss}^S}{2}\right]\hat{S}+i\sqrt{\Gamma_S}\hat{\mathcal{E}}_0(0,t)+\hat{F}_S(t), \tag{7}$$

with $(\Gamma_S,\gamma_{\rm loss}^S,\Delta_s)=\rho\times(\Gamma,\gamma_{\rm loss},\delta_p-\Delta)$, and $\rho(t)=\left|\frac{-i\Omega^*(t)}{(\Gamma+\gamma_{\rm loss})/2-i(\delta_p-\Delta)}\right|^2$. Notably, this equation has exactly the same form of Eq. (1) for $\hat{P}$, with an identical reflectivity parameter $r_0=\Gamma_S/(\Gamma_S+\gamma_{\rm loss}^S)=\Gamma/(\Gamma+\gamma_{\rm loss})$ that should characterize its atom-photon excitation transfer.

Indeed, we analyzed the quantum memory protocol for this model in close analogy to that in Ref. [16] for an atomic ensemble inside an optical cavity in the fast cavity regime. We present the details of this analysis in Appendix B, including the expressions for the control-pulse temporal shape $\Omega(t)$ needed for optimal storage (retrieval), given the temporal shape of the input (output) photon wave packet one wishes to store (retrieve). We find that the optimal storage and retrieval efficiencies are both equal to r_0, reflecting that these are time-reversed processes [16]. The meaning, revealed by our approach, is that the on-resonance reflectivity $r_0=|r(\delta_p=\Delta)|$ is in fact equal to the quantum

memory efficiency. As shown above, this in turn stems from the light-matter coupling efficiency of the underlying scattering problem. In particular, the total efficiency of the quantum memory is given by the multiplication of the storage and retrieval efficiencies, r_0^2, which is nothing but the intensity reflectivity. Thus, the memory protocol, using the temporal tunability of the coupling field $\Omega(t)$, allows one to break the reflection process into two distinct stages: absorption (storage) and re-emission (retrieval). But the combined effect is equivalent to intensity reflection, as exhibited by the total coupling efficiency r_0^2.

2. Quantum correlation efficiency: Squeezing

Correlated states of atoms or photons are useful in, e.g., quantum metrology and quantum information processing, and typically require nonlinearities of the atomic system to generate them [2,17]. To this end, we introduce a nonlinear variant of the model (1) by simply adding a nonlinear term in $\hat{P}$ to the equation for $d\hat{P}/dt$, while still keeping $\hat{P}$ as a linearized boson mode. For example, for a cubic Kerr-type nonlinearity we have

$$\frac{d\hat{P}}{dt} = \left[i(\delta_p - \Delta) - \frac{\Gamma + \gamma_{\rm loss}}{2}\right]\hat{P} - iV\hat{P}^\dagger\hat{P}^2 + i\sqrt{\Gamma}\hat{\mathcal{E}}_0(0,t) + \hat{F}(t), \tag{8}$$

where V is the nonlinearity parameter associated with an interaction potential within the atomic system. For an atomic system within its linear regime, which can be mapped to the 1D model (1), the mapping to the above 1D model (8) in the presence of nonlinearities is not always possible, since interactions and nonlinearities typically couple different spatial modes in the transverse directions (x-y plane), thus going beyond a single-channel, 1D picture. However, we discuss in Appendix C common situations wherein the model (8) does capture the nonlinear dynamics of the target mode of interest. In particular: (i) considering an interaction potential $V(r_a)$ between atomic excitations on different atoms at a distance r_a from each other, if the potential is effectively uniform within the atomic system (as can be realized with Rydberg dressing [18,19]), then $V(r_a) = V$ does not couple different transverse modes and conserves the 1D picture; (ii) for two-level atoms, where the saturation of atoms yields an on-site potential, if the excitation is weak enough, the nonlinearity becomes perturbative, resulting in a negligible effect of other transverse modes on the target mode, thus yielding the model (8).

We now turn to analyze quantum-squeezing correlations, useful e.g. in quantum metrology, generated both in the atomic system and the output light. We consider the model (8) with a weak coherent-state input field of average amplitude $\langle\hat{\mathcal{E}}_0(0,t)\rangle = \overline{\mathcal{E}}$, and we solve for the steady-state perturbatively in $\overline{\mathcal{E}}$. For the atomic system, treating $\hat{P}$ as a collective-spin variable of many two-level atoms, the bosonic squeezing parameter ξ_P^2 amounts to spin squeezing, and we find $\xi_P^2 \approx 1 - r_0\frac{|\overline{\mathcal{E}}|^2}{\Gamma+\gamma_{\rm loss}}f(V)$, where $f(V)$ is a function of V (see Appendix C). Quantum-squeezing correlations exist for $\xi_P^2 < 1$. Therefore, the second term characterizes the strength of quantum correlations and is seen to be proportional to r_0. Similarly, for the quantum squeezing parameter of the output field, we obtain $\xi_E^2 \approx 1 - r_0^2\frac{|\overline{\mathcal{E}}|^2}{[\hat{\mathcal{E}}_0(t),\hat{\mathcal{E}}_0^\dagger(t)]}f(V)$. So, for the light we get that the strength of quantum correlations is multiplied by another factor of r_0, since atomic correlations are converted to light, resulting in an overall proportionality with the intensity reflectivity r_0^2. Therefore, as anticipated above, while efficiencies of nonlinear quantum tasks (here strength of generated correlations) may involve more parameters (e.g., V), they also must be proportional to the reflectivity r_0 (or r_0^2), which is the ultimate parameter quantifying light-matter coupling within a 1D-like system. Furthermore, we expect this general idea to apply to various mechanisms of array nonlinearity: e.g., in Ref. [36], where array nonlinearity originates only from an optomechanical effect, the generated photon correlations were also shown to scale as the reflectivity.

3. Quantum correlation efficiency: Photon blockade

An even simpler form of nonlinearity is also the strongest one; namely, that where the atomic system is effectively allowed to have only a single excitation, due to strong interactions, $V \to \infty$ in Eq. (8). Such strong nonlinearities lead to photon-photon interactions and correlations that are useful e.g. in photonic quantum gates [2], and can be simply modeled by an atomic system with a single excited level and a single ground level. For a single atom, this amounts to a two-level atom model, whereas for an atomic ensemble, e.g., an array, a similar situation is achieved via Rydberg blockade [60,61]. In the latter, we consider a third atomic level of each atom, $|s\rangle$, taken as a highly excited, metastable Rydberg state, forming a ladder system with $\delta_2 = \delta_p + \delta_c$ [Fig. 1(c)]. For strong enough interaction between Rydberg states of different atoms (large blockade radius [61,62]), all multiply excited states of the form $(\hat{S}^\dagger)^n|gg\ldots g\rangle$ $(n > 1)$ are far detuned and truncated [55] (where here again $\hat{S}$ is the collective coherence associated with $|g\rangle$ and $|s\rangle$).

As in Sec. II D 1, we adiabatically eliminate $\hat{P}$, obtaining Eq. (7) for $\hat{S}$, however this time together with the blockade condition $(\hat{S}^\dagger)^n|gg\ldots g\rangle = 0$ $(n > 1)$. This amounts to a problem involving scattering off a single two-level emitter in one dimension, equivalent to the model (8) with $V \to \infty$. Following Ref. [55], where the specific problem of a formally infinite 2D array was treated, we solve this general nonlinear problem analytically: Given a coherent-state input, we find the steady-state photon correlations of

the output light. For example, at the resonances $\delta_2 = 0$ and $\delta_p = \Delta$, we obtain antibunching for the transmitted light, with $g^{(2)}(0) = |1 - r_0^2|^2$. This expression clearly demonstrates that it is again the reflectivity of the array that determines the amount of correlations, as was also suggested by the numerical results in Refs. [52,53], where the utility of such correlations for two-qubit gates was discussed. In Ref. [55], a similar conclusion was reached also for the entanglement generated between different transverse modes scattered off a 2D array. The photon blockade problem thus forms an example of a nonlinear problem wherein no additional parameters beyond r_0 appear (unlike the case of a finite nonlinearity V). Then the efficiency of entanglement generation in this quantum nonlinear problem is given by the efficiency of the underlying classical linear problem, namely, r_0.

E. Why reflectivity? Consequences and relation to other figures of merit

The considerations presented above establish that the on-resonance reflectivity r_0 forms a figure of merit for the efficiency of the generic, two-sided 1D quantum interface. This idea has an important practical meaning: for any given symmetric two-sided system that is mapped onto the generic 1D model of Eq. (1) [or Eqs. (6) and (8)], the efficiencies of relevant quantum problems are given by a well-defined and measurable physical quantity, the linear reflectivity r_0. The latter can be directly extracted from the measurement, or the simple classical calculation, of the field reflected off the atomic system.

So, for symmetric, two-sided quantum interfaces, we argue that the reflectivity is the natural and physically meaningful figure of merit to consider, and this is the basis of the approach we present. However, mathematically, r_0 is clearly related to other figures of merit that exist in the literature. First and foremost, we defined the cooperativity C in Eq. (2) as a general ratio between rates of decay to desired (Γ) and undesired ($\gamma_{\rm loss}$) modes. This definition coincides with the known definitions of cooperativity when the losses to undesired modes arise from free-space like emission at the individual-atom level (noncollective), i.e., $\gamma_{\rm loss} = \gamma$. For example, in cavity QED of dilute atomic ensembles, the transverse emission from atoms inside the cavity to the nonconfined modes is approximately given by the individual-atom free-space decay rate, $\gamma_{\rm loss} = \gamma$, whereas the emission via the cavity mirrors is $\Gamma \propto \gamma \mathcal{F} \lambda^2 / A_c$, with $\mathcal{F}$ being the cavity finesse and A_c its mode area [2]. In waveguide QED a similar definition exists, where again $\gamma_{\rm loss} = \gamma$ is the emission to nonguided modes and $\Gamma \propto \gamma \lambda^2 / A_{\rm wg}$, with $A_{\rm wg}$ the area of the guided mode, yielding the so-called β factor of waveguide QED, $\beta = C/(C+1) = r_0$ [58,59,63]. Therefore, these known definitions coincide with ours only when the loss rate does not consider collective effects in the loss to undesired modes. In contrast, in the situations we consider below, such as atomic arrays, the losses are very much affected by collective physics [37], and so these common definitions, wherein $\gamma_{\rm loss} = \gamma$, are not appropriate: for example, this means that the β factor is not equal to the reflectivity one measures in such a case.

Another common definition from the literature is the OD [12,64]. Although similar in essence to the cooperativity, the observable physical meaning of OD is revealed in one-sided propagation problems, where back-reflection is negligible and $e^{-\rm OD}$ expresses the extinction of the field in transmission. We, instead, consider problems where back-propagation is very crucial, as we deal with two-sided, symmetric problems. As we show below, propagation problems in elongated atomic systems that can be mapped to our two-sided 1D model satisfy a Bragg condition that guarantees back-reflection. In such cases, the OD does not characterize the system well, and the suitable, physically meaningful figure of merit is the reflectivity r_0 introduced here.

III. MAPPING A COLLECTIVE SYSTEM TO THE 1D MODEL

We now turn to developing a method for the mapping of a collective atom-photon system to the generic 1D model. Starting from the Heisenberg-Langevin equations of a many-atom system interacting with free-space photons modes, we find existence conditions for the mapping and provide the procedure to perform it. In this section we focus on a planar atomic system in its linear regime; extensions accounting for multiple planar layers and for nonlinearities are developed in Sec. VII and Appendix C 2, respectively.

A. System

We consider a collection of identical three-level atoms [Fig. 1(c)], $n = 1, \ldots, N$, situated at fixed positions $\mathbf{r}_n = (\mathbf{r}_n^\perp, z_n)$ ($\mathbf{r}_\perp$ and z denoting projections along transverse x-y and longitudinal z directions). The atoms are illuminated by a quantum field with central frequency ω_p working on the $|g\rangle \leftrightarrow |e\rangle$ transition, while an external coherent field $\Omega(t)$ with frequency ω_c couples the levels $|s\rangle \leftrightarrow |e\rangle$ [Fig. 1(b)]. The full Hamiltonian is given by

$$\hat{H} = \hat{H}_f + \hat{H}_s + \hat{H}_I. \tag{9}$$

Here $\hat{H}_f = \sum_{\mathbf{k}_\perp} \sum_{k_z} \sum_\mu \hbar \omega_{\mathbf{k}_\perp k_z} \hat{a}^\dagger_{\mathbf{k}_\perp k_z \mu} \hat{a}_{\mathbf{k}_\perp k_z \mu}$ is the Hamiltonian of the photons in free space, with boson lowering operators $\hat{a}_{\mathbf{k}_\perp k_z \mu}$ characterized by the transverse and longitudinal wave vectors $\mathbf{k}_\perp = (k_x, k_y)$ and k_z, respectively, the polarization index μ, and $\omega_{\mathbf{k}_\perp k_z} = c\sqrt{|\mathbf{k}_\perp|^2 + k_z^2}$. The

Hamiltonian of the atomic system is

$$\hat{H}_s = \sum_n \left[\hbar\omega_e \hat{\sigma}_{ee,n} + \hbar\omega_s \hat{\sigma}_{ss,n}\right] - \left[\hbar\Omega e^{-i\omega_c t}\hat{\sigma}^\dagger_{se,n} + \text{H.c.}\right], \tag{10}$$

where $\hat{\sigma}_{\alpha\alpha',n} = |\alpha\rangle_n\langle\alpha'|$ and $\hbar\omega_\alpha$ are the transition operator (of an atom n) and energy, respectively, of levels $\alpha, \alpha' \in \{g, e, s\}$. The atom-photon interaction Hamiltonian in the dipole approximation reads

$$\hat{H}_I = -\sum_n \left[\mathbf{d}_{ge}\hat{\sigma}_{ge,n} + \mathbf{d}_{se}\hat{\sigma}_{se,n} + \text{H.c.}\right] \cdot \left[\hat{\mathbf{E}}(\mathbf{r}_n^\perp, z_n) + \text{H.c.}\right], \tag{11}$$

where $\mathbf{d}_{ge} = d\mathbf{e}_d$ is the dipole matrix element corresponding to the $|g\rangle \leftrightarrow |e\rangle$ transition and $\mathbf{d}_{se}$ corresponds to the $|s\rangle \leftrightarrow |e\rangle$ transition. The quantum field operator is given by

$$\hat{\mathbf{E}}(\mathbf{r}_\perp, z, t) = i\sum_{\mathbf{k}_\perp}\sum_{k_z}\sum_{\mu}\sqrt{\frac{\hbar\omega_{\mathbf{k}_\perp k_z}}{2\epsilon_0 L^3}}\mathbf{e}_{\mathbf{k}_\perp k_z \mu}\hat{a}_{\mathbf{k}_\perp k_z \mu}(t) \times e^{i(\mathbf{k}_\perp\cdot\mathbf{r}_\perp + k_z z)}, \tag{12}$$

with L^3 being the quantization volume and $\mathbf{e}_{\mathbf{k}_\perp k_z \mu}$ the photon polarization vector.

B. Heisenberg-Langevin formalism

Writing the Heisenberg equation for the photons in the laser-rotated frame ($\hat{\sigma}_{ge,n}e^{i\omega_p t} \to \hat{\sigma}_{ge,n}$, $\hat{\sigma}_{gs,n}e^{i(\omega_p-\omega_c)t} \to \hat{\sigma}_{gs,n}$), we solve for the photon field under the Born-Markov approximation, obtaining

$$\hat{E}(\mathbf{r}_\perp, z) = \hat{E}_0(\mathbf{r}_\perp, z) + \frac{\omega_p^2 d}{\epsilon_0 c^2}\sum_n G(\omega_p, \mathbf{r}_\perp - \mathbf{r}_n^\perp, z - z_n)\hat{\sigma}_{ge,n}. \tag{13}$$

Here $\hat{E}(\mathbf{r}_\perp, z) = \mathbf{e}_d^* \cdot \hat{\mathbf{E}}(\mathbf{r}_\perp, z)e^{i\omega_p t}$ is the slowly varying envelope of the field around a carrier frequency ω_p and projected onto the transition-dipole orientation $\mathbf{e}_d$, whereas $\hat{E}_0(\mathbf{r}_\perp, z)$ is the corresponding freely evolving input field [given by Eq. (12) with $\hat{a}_{\mathbf{k}_\perp k_z \mu}(t) \to \hat{a}_{\mathbf{k}_\perp k_z \mu}(0)e^{-i\omega_{\mathbf{k}_\perp k_z}t}$]. $G(\omega, \mathbf{r}_\perp, z)$ is the (dyadic) Green's function of the photon field in free space at frequency ω, also projected onto the dipole orientation. The total field is then given by a superposition of the incoming field and that emitted by the atoms and propagated via the Green's function.

Under the same Born-Markov approximation, we integrate out the photonic operators and derive the Heisenberg-Langevin equations for the atomic operators. Linearizing the equations in the weak quantum field (e.g., see the appendix in Ref. [55]), we obtain

$$\frac{d\hat{\sigma}_{ge,n}}{dt} = -\left(\frac{\gamma_s}{2} - i\delta_p\right)\hat{\sigma}_{ge,n} + i\Omega(t)\hat{\sigma}_{gs,n} + \frac{id}{\hbar}\hat{E}_0(\mathbf{r}_n^\perp, z_n) + \hat{F}_n + \frac{i}{\hbar}\frac{d^2\omega_p^2}{\epsilon_0 c^2}\sum_m G(\omega_p, \mathbf{r}_n^\perp - \mathbf{r}_m^\perp, z_n - z_m)\hat{\sigma}_{ge,m}, \tag{14}$$

$$\frac{d\hat{\sigma}_{gs,n}}{dt} = i\delta_2\hat{\sigma}_{gs,n} + i\Omega^*(t)\hat{\sigma}_{ge,n}. \tag{15}$$

Here γ_s is a spontaneous decay rate due to noncollective processes: it may include a decay γ_{se} from $|e\rangle$ to $|s\rangle$ and a noncollective decay due to other imperfections, e.g., position disorder in the case of atomic arrays (see below). $\hat{F}_n$ is the corresponding quantum Langevin noise operator satisfying $\langle\hat{F}_n(t)\hat{F}_m^\dagger(t')\rangle = \gamma_s\delta_{nm}\delta(t-t')$. $\delta_p = \omega_p - \omega_e$ is the detuning of the $|g\rangle \leftrightarrow |e\rangle$ transition and $\delta_2 = \delta_p - \delta_c$ is the two-photon detuning, with $\delta_c = \omega_c - (\omega_e - \omega_s)$ being the detuning of the $|s\rangle \leftrightarrow |e\rangle$ transition [Fig. 1(b)]. The Green's function in Eq. (14) describes the dipole-dipole interaction between the $|g\rangle \leftrightarrow |e\rangle$ transition dipoles of pairs of atoms n and m; such a term is absent between the $|s\rangle \leftrightarrow |e\rangle$ transition dipoles of different atoms since in the linear regime the probability of exciting two atoms to states $|s\rangle$ and $|e\rangle$ is low [55].

C. The target photon mode

We consider incident light propagating along the z direction with a transverse mode profile $u(\mathbf{r}_\perp)$, satisfying the normalization $\int_{-\infty}^{\infty}|u(\mathbf{r}_\perp)|^2 d\mathbf{r}_\perp = 1$. For a paraxial beam, the typical scale of spatial variations of $u(\mathbf{r}_\perp)$, denoted by w, is much larger than the optical wavelength $\lambda = 2\pi c/\omega_p$. We define the field projected to this mode as

$$\hat{E}_u(z) \equiv \frac{1}{\sqrt{A_u}}\int_{-\infty}^{\infty}\hat{E}(\mathbf{r}_\perp, z)u^*(\mathbf{r}_\perp)d\mathbf{r}_\perp = i\sum_{k_z}\sqrt{\frac{\hbar\omega_{k_z}}{2\epsilon_0 L A_u}}\hat{a}_{uk_z}e^{i(k_z z + \omega_p t)}, \tag{16}$$

where A_u is an unimportant area scale associated with the mode. The second equality, appearing as an expansion in one-dimensionally-propagating waves, is obtained within the paraxial approximation by introducing the 1D continuum of annihilation operators associated with the transverse mode $u(\mathbf{r}_\perp)$, $\hat{a}_{uk_z} = (2\pi/L)\sum_{\mathbf{k}_\perp}\sum_\mu \mathbf{e}_d^* \cdot \mathbf{e}_{\mathbf{k}_\perp k_z \mu}\hat{a}_{\mathbf{k}_\perp k_z}\tilde{u}^*(\mathbf{k}_\perp)$, with $\tilde{u}(\mathbf{k}_\perp)$ being the Fourier transform of $u(\mathbf{r}_\perp)$, and $[\hat{a}_{uk_z}, \hat{a}^\dagger_{uk'_z}] = \delta_{k_z,k'_z}$.

For a paraxial mode $u(\mathbf{r}_\perp)$ of spatial width $w \gg \lambda$, and considering propagation distances within its Rayleigh range, $z < z_R = \pi w^2/\lambda$, diffraction of the mode is negligible and its propagation along z is expected to be that of an

effective plane wave in one dimension. Indeed, performing the projection (16) on the field equation (13), we show in Appendix D 1 that for $w \gg \lambda$ and $z < z_R$, one obtains

$$\hat{E}_u^{\pm}(z) = \hat{E}_{u,0}^{\pm}(z) + e^{\pm ik_p z}\frac{idk_p}{2\epsilon_0\sqrt{A_u}}\sum_n u^*(\mathbf{r}_n^{\perp})e^{\mp ik_p z_n}\hat{\sigma}_{ge,n}. \tag{17}$$

Here $k_p = \omega_p/c = 2\pi/\lambda$, whereas $\hat{E}_u^+(z)$ and $\hat{E}_u^-(z)$ are the right- and left-propagating fields [including only $k_z > 0$ or $k_z < 0$, respectively, in Eq. (16)], sampled at $z > z_{\max}$ and $z < z_{\min}$, respectively ($z_n \in [z_{\min}, z_{\max}]$).

We identify that $E_u^{\pm}$ are coupled to $\hat{P}_{\pm} \propto \sum_n u^*(\mathbf{r}_n^{\perp})$ $e^{\mp ik_p z_n}\tilde{\sigma}_{ge,n}$. However, for a mapping to Eq. (4) of the two-sided 1D model, we need a single dipole mode $\hat{P} = \hat{P}_+ = \hat{P}_-$. A simple way to achieve this is by demanding that $e^{ik_p z_n} = e^{-ik_p z_n}$, or

$$z_n = (\lambda/2) \times \mathbb{N} \quad \forall n. \tag{18}$$

From now on we assume a planar system, for which $z_n = 0\ \forall n$. The extension of the formalism to 3D structures is discussed in Sec. VI.

D. The collective dipole in a planar system

The considerations above establish the natural "candidate" for the relevant collective dipole in a planar system given by

$$\hat{P} = a_{\text{eff}}\sum_n u^*(\mathbf{r}_n^{\perp})\hat{\sigma}_{ge,n}. \tag{19}$$

The normalization length a_{eff} is defined through

$$\sum_n |u(\mathbf{r}_n^{\perp})|^2 = 1/a_{\text{eff}}^2, \tag{20}$$

guaranteeing the bosonic commutation relation $[\hat{P}, \hat{P}^{\dagger}] = 1$ within the linear regime taken here. We now turn to writing the equation of motion for $\hat{P}$ and identifying the conditions under which it can be mapped to that of the 1D model of Eq. (1). To this end, we first introduce the eigenvectors $v_{l,n}$ with eigenvalues D_l of the dipole-dipole interaction kernel, $D_{nm} \equiv -\frac{i}{\hbar}\frac{d^2\omega_p^2}{\epsilon_0 c^2}G(\omega_p, \mathbf{r}_n^{\perp} - \mathbf{r}_m^{\perp}, 0)$,

$$\sum_m D_{nm}v_{l,m} = D_l v_{l,n}, \quad D_{nm} = \sum_l v_{l,n}v_{l,m}D_l, \tag{21}$$

noting the orthogonality and completeness relations of eigenvectors of the complex symmetric matrix D_{nm}, $\sum_n v_{l,n}v_{l',n} = \delta_{ll'}$, $\sum_l v_{l,n}v_{l,m} = \delta_{nm}$. Writing Eq. (14) for $\hat{P}$ using Eqs. (19) and (21), we find

$$\frac{d\hat{P}}{dt} = \left(i\delta_p - \frac{\gamma_s}{2}\right)\hat{P} + i\Omega\hat{S} + i\frac{d}{\hbar}\hat{E}_0 + \hat{F}_u - a_{\text{eff}}\sum_l D_l\sum_m v_{l,m}\tilde{\sigma}_{ge,m}\sum_n u^*(\mathbf{r}_n^{\perp})v_{l,n}. \tag{22}$$

Here $\hat{S} = a_{\text{eff}}\sum_n u^*(\mathbf{r}_n^{\perp})\hat{\sigma}_{gs,n}$ is the collective coherence defined as in Eq. (19) with the replacement $\hat{\sigma}_{ge,n} \to \hat{\sigma}_{gs,n}$, and $\hat{E}_0$ and $\hat{F}_u$ are similarly transformed via Eq. (19) from $\hat{E}_0(\mathbf{r}_n^{\perp}, z_n)$ and $\hat{F}_n$, respectively.

The last term describes the coupling of the collective dipole $\hat{P}$ to dipole eigenmodes of the form $\hat{P}_l = \sum_m v_{l,m}\tilde{\sigma}_{ge,m}$. Coupling of $\hat{P}$ to other dipole modes prevents the mapping to the single-mode 1D model (1). This can be remedied if the target mode is equal to one specific dipole eigenmode $l = 0$, or if it overlaps only with quasidegenerate eigenmodes l with $D_l \approx D_0$, i.e.,

$$a_{\text{eff}}u^*(\mathbf{r}_n^{\perp}) = v_{0,n}, \quad \text{or} \quad a_{\text{eff}}u^*(\mathbf{r}_n^{\perp}) = \sum_{l\in(D_l\approx D_0)} c_l v_{l,n}, \tag{23}$$

with $\sum_{l\in(D_l\approx D_0)}|c_l|^2 = 1$. In either case, Eq. (22) becomes

$$\frac{d\hat{P}}{dt} = \left[i(\delta_p - \Delta) - \frac{\Gamma_0 + \gamma_s}{2}\right]\hat{P} + i\Omega\hat{S} + i\frac{d}{\hbar}\hat{E}_0 + \hat{F}_u, \tag{24}$$

where we have already decomposed D_0 to real and imaginary parts, $D_0 = \Gamma_0/2 + i\Delta$, corresponding to collective decay and energy shift, respectively. Moreover, applying the transformation (19) on Eq. (15), we trivially obtain

$$\frac{d\hat{S}}{dt} = i\delta_2\hat{S} + i\Omega^*(t)\hat{P}. \tag{25}$$

E. Mapping to the 1D model

The input-field term $\hat{E}_0 = a_{\text{eff}}\sum_n u^*(\mathbf{r}_n^{\perp})\hat{E}_0(\mathbf{r}_{\perp}, 0)$ contains the overlap with the target mode but possibly also with other photon modes. Using a complete function basis that spans the transverse x-y plane, we decompose the field to the target mode component $u(\mathbf{r}_{\perp})$ and other orthogonal modes (see Appendix D 2), obtaining

$$i\frac{d}{\hbar}\hat{E}_0 = i\sqrt{\Gamma}\hat{\mathcal{E}}_0(0) + \hat{F}_0. \tag{26}$$

Here

$$\hat{\mathcal{E}}(0) = \frac{1}{\sqrt{2}}(\hat{\mathcal{E}}_+(0) + \hat{\mathcal{E}}_-(0)), \quad \hat{\mathcal{E}}_{\pm}(z) \equiv \frac{d}{\hbar}\sqrt{\frac{2A_u}{a_{\text{eff}}^2\Gamma}}\hat{E}_u^{\pm}(z), \tag{27}$$

is the (normalized) input field at the target mode, written as a symmetric superposition of right- and left-propagating

fields, and $\hat{F}_0$ is a noise operator due to the vacuum field containing other modes. The effective 1D coupling strength of the target mode to $\hat{P}$ is seen to be given by Γ, which we find to be equal to Γ_{1D}, the emission rate in a 1D system with a transverse cross section of $a_{\rm eff}^2$ (see Appendix D 2),

$$\Gamma = \Gamma_{1D}, \quad \Gamma_{1D} = \frac{d^2\omega_p}{\epsilon_0\hbar c a_{\rm eff}^2} = \frac{3}{4\pi}\frac{\lambda^2}{a_{\rm eff}^2}\gamma, \quad \gamma = \frac{d^2\omega_p^3}{3\pi\epsilon_0\hbar c^3}, \tag{28}$$

where γ is the usual free-space spontaneous emission rate of a single atom ($|g\rangle \leftrightarrow |e\rangle$ transition).

We observe that while $\hat{P}$ in Eq. (24) exhibits a collective decay Γ_0, its coupling to the target mode is characterized by Γ. We therefore divide Γ_0 into Γ and $\Gamma_0 - \Gamma$, with the latter expressing the fraction of the collective emission that is not coupled to the target mode, and where we prove that $\Gamma_0 \geq \Gamma$ (see Appendix D 3). Therefore, the total emission outside of the target mode is given by the sum of the latter and the noncollective emission γ_s, yielding

$$\frac{d\hat{P}}{dt} = \left[i(\delta_p - \Delta) - \frac{\Gamma + \gamma_{\rm loss}}{2}\right]\hat{P} + i\Omega\hat{S} + i\sqrt{\Gamma}\hat{\mathcal{E}}_0(0) + \hat{F}, \tag{29}$$

with

$$\gamma_{\rm loss} = (\Gamma_0 - \Gamma) + \gamma_s \geq \gamma_s, \quad \frac{\Gamma_0}{2} + i\Delta = D_0. \tag{30}$$

Correspondingly, the Langevin noise $\hat{F} = \hat{F}_0 + \hat{F}_u$ comprises noise due to these two loss effects and it satisfies $\langle \hat{F}(t)\hat{F}^\dagger(t')\rangle = \gamma_{\rm loss}\delta(t-t')$.

With the collective dipole $\hat{P}$ in hand, we write also the field equation (17) in a diagonalized form:

$$\hat{\mathcal{E}}_\pm(z) = \hat{\mathcal{E}}_{0\pm}(z) + i\sqrt{\frac{\Gamma}{2}}e^{\pm ik_p z}\hat{P}. \tag{31}$$

The scattered field propagates symmetrically on both sides of the array, so similarly to the input field, we define the output symmetric field $\hat{\mathcal{E}}(z)$ as a symmetric superposition of the right- and left-propagating fields: $\hat{\mathcal{E}}(z) = \frac{1}{\sqrt{2}}\left[\hat{\mathcal{E}}_+(z) + \hat{\mathcal{E}}_-(-z)\right]e^{-ik_p z}$ $(z > 0)$. The input-output relation for this symmetric field then reads

$$\hat{\mathcal{E}}(z) = \hat{\mathcal{E}}_0(z) + i\sqrt{\Gamma}\hat{P}. \tag{32}$$

This equation reveals the mode-preserving light-matter coupling: input light $\hat{\mathcal{E}}_0$ at the target mode $u(\mathbf{r}_\perp)$ excites the corresponding collective dipole mode $\hat{P}$, which will finally be emitted as output light $\hat{\mathcal{E}}$ of the same target mode.

F. Conclusion

We identify that Eqs. (29), (32), and (25) establish the mapping to the 1D model, Eq. (1) [or Eq. (6)], with the model parameters Γ and $\gamma_{\rm loss}$ given in Eqs. (28) and (30). The paraxial target mode defines the collective dipole $\hat{P}$ and the effective length $a_{\rm eff}$ in Eqs. (19) and (20), respectively, with the condition that it must be spatially matched to a dipole eigenmode as in Eq. (23). The latter condition can be satisfied only if the spatial structure of the atomic system supports an eigenmode that corresponds to a paraxial beam. We see below that this is indeed the case for various arraylike structures, even beyond the purely translation-invariant structures.

IV. EXAMPLE 1: 2D ORDERED ARRAYS

As a first application of our approach, we derive useful new analytical results for a familiar case, the 2D square array. The results are summarized in Tables I and II and consist of the mapping parameters Γ and $\gamma_{\rm loss}$ of the 1D model, for a typical case of a Gaussian-beam target mode and finite-size, nonideal 2D arrays.

Before we sketch the derivation and present the results, we begin with some useful intuition on why a 2D ordered array can be mapped to the 1D model. Considering first an infinite 2D ordered array, the lattice translation invariance imposes that the dipole eigenmodes are 2D lattice Fourier modes, $l \to \mathbf{k}_\perp$. Then a paraxial, Gaussian-beam target mode with a very large waist $w \gg \lambda$ spatially overlaps with dipole modes of a very small wave vector $|\mathbf{k}_\perp| < 2\pi/w \to 0$. The latter can become quasidegenerate for the relevant timescales, $D_{\mathbf{k}_\perp} \approx D_{\mathbf{k}_\perp=0}$ [46], thus allowing the mapping to the 1D model. Considering finite-size arrays, this reasoning still holds if the array is large enough, as we show below. This allows us to establish the mapping to the 1D model also including finite-size effects and imperfections.

A. System

We consider a 2D array of identical atoms forming a square lattice on the x-y plane with lattice spacing a (Fig. 2). Most of the discussion is dedicated to arrays whose lattice spacing a is smaller than the relevant optical wavelength $\lambda = 2\pi c/\omega_p$, as is typical of an optical lattice realization [25,26,30], whereas towards the end we also briefly comment on the case $a > \lambda$, relevant to optical tweezer arrays [56,57]. The atomic positions are given by the 2D lattice points, $z_n = 0$ and $\mathbf{r}_n^\perp = \mathbf{r}_{n_x,n_y}^\perp = a(n_x, n_y)$ (n_x and n_y being integers). Imperfections due to small spatial disorder δr in the array atomic positions are accounted for by supplementing the noncollective decay term γ_s in Eq. (14) with the scattering rate $\gamma_{\rm dis} \propto (\delta r/\lambda)^2$ [29,46], leading to $\gamma_s = \gamma_{se} + \gamma_{\rm dis}$ (see further discussion in Sec. IV C). We note that the decay rate γ_{se} of the

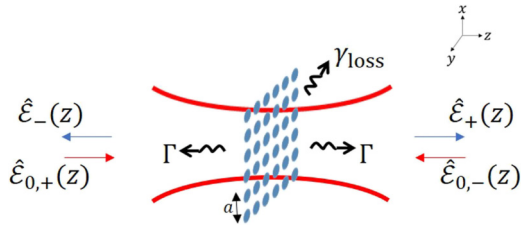

FIG. 2. 2D ordered array. A finite-size array with lattice spacing a is situated on the x-y plane ($z = 0$). The target-mode input consists of the symmetric combination of fields from both sides, $\hat{\mathcal{E}}_{0,\pm}$. The full free-space multimode problem is mapped to the generic model in Fig. 1(a), with the relevant field and collective dipole modes projected to the target-mode profile [Eqs. (16) and (19)] and with the effective parameters Γ and γ_{loss} from Table I.

$|s\rangle \leftrightarrow |e\rangle$ transition may become negligible, e.g., in a ladder-type atomic configuration [Fig. 1(c)] where $|s\rangle$ is a highly excited metastable level (e.g., Rydberg state).

B. Mapping to the 1D model

The array is illuminated from both sides by a paraxial target mode with a normalized transverse profile $u(\mathbf{r}_\perp)$, as defined in Eq. (16). A typical case is a Gaussian beam $u(\mathbf{r}_\perp) = \sqrt{(2/\pi w^2)}e^{-(\mathbf{r}_\perp)^2/w^2}$, with $w \gg \lambda$. Following the general formalism presented in Sec. III, we expect that the relevant collective dipoles will follow the same spatial structure.

In Appendix E we show that the dipole mode $\hat{P}$ from Eq. (19) of our general formalism, which matches the spatial profile $u(\mathbf{r}_\perp)$ of the target-mode field $\hat{\mathcal{E}}$, approximately diagonalizes the dipole-dipole kernel in Eq. (14). This is valid under the following reasonable assumptions: (i) $L_a = a\sqrt{N} \gg \lambda$, i.e., the linear size of the array is larger than the length scale associated with the dipole-dipole interaction (λ), so each atom in the "bulk" (not at the edges) effectively feels interactions of an infinite array; (ii) $\sqrt{N} \gg 1$, so most atoms are in the bulk, and edge atoms are negligible in describing collective dipole modes. With these two assumptions, the collective shift and width are well approximated by those of a uniformly excited infinite array, $\Delta \equiv \Delta_{\mathbf{k}_\perp=0}$ (see Appendix E), and

$$\Gamma_0 \equiv \Gamma_{\mathbf{k}_\perp=0} = \frac{3}{4\pi}\frac{\lambda^2}{a^2}\gamma. \tag{33}$$

Effects due to the finite size of the array are captured here by its nonperfect overlap with the target mode, as we now show. The normalization length a_{eff} from Eq. (20) is given in a 2D array by

$$a_{\text{eff}} = \frac{a}{\sqrt{\eta}},$$
$$\eta = \int_{L_a^2} d\mathbf{r}_\perp |u(\mathbf{r}_\perp)|^2 \xrightarrow[\text{Gaussian}]{} \eta = \text{erf}^2\left(\frac{L_a}{\sqrt{2}w}\right), \tag{34}$$

TABLE I. Mapping of ordered-array interfaces to the generic 1D model in Fig. 1 and Sec. III (model parameters Γ and γ_{loss}). For a 2D array (N atoms, lattice constant a) the collective coupling rate Γ_0 to the target mode is reduced by the overlap factor $\eta = \text{erf}^2\left(\frac{a\sqrt{N}}{\sqrt{2}w}\right) < 1$ between the target-mode profile (e.g., a Gaussian of waist w) and the finite-size array. Here γ is the individual-atom free-space spontaneous emission rate. For lattice spacing exceeding the wavelength, $a > \lambda$, losses due to scattering to higher diffraction orders occur [γ_{diff}, Eq. (36)], in addition to individual-atom losses (γ_s, e.g., due to disorder) and those due to nonperfect spatial overlap [$(1-\eta)\Gamma_0$]. For 3D arrays, phase-matching conditions enhance collective emission by a factor of N_z (the number of layers, Fig. 8): for good overlap $\eta \to 1$, the cooperativity $C = \Gamma/\gamma_{\text{loss}}$ also increases by N_z. Comparing these free-space array cases with a dilute atomic ensemble inside a cavity (e.g., Ref. [16]), we observe a similar scaling of the coupling Γ (noting that $\sim N/w^2$ is the effective 2D density in analogy to N_z/a^2 of the array), but with an enhancement of $\mathcal{F}$ from the cavity finesse. The cavity enhancement $\mathcal{F}$ is required for a dilute ensemble to combat its large losses arising from individual-atom transverse scattering out of the cavity at rate $\gamma \sim \Gamma_0$ [compared with much smaller losses of ordered arrays, $(1-\eta)\Gamma_0$, γ_s; see Table II].

	Emission rate to target mode Γ	Emission rate to undesired modes γ_{loss}
2D atom array $a < \lambda$ (Sec. V)	$\eta\Gamma_0 = \eta\frac{3}{4\pi}\frac{\lambda^2}{a^2}\gamma$	$(1-\eta)\Gamma_0 + \gamma_s$
2D atom array $a > \lambda$ (Sec. V)		$(1-\eta)\Gamma_0 + \gamma_s + \gamma_{\text{diff}}$
3D atom array $a < \lambda$ (Sec. VI)	$\eta N_z\Gamma_0 = \eta\frac{3}{4\pi}\frac{\lambda^2}{a^2}N_z\gamma$	$(1-\eta)N_z\Gamma_0 + \gamma_s$
Cavity (reference case)	$\frac{3}{4\pi}\frac{\lambda^2}{\pi w^2/2}N\frac{4}{\pi}\mathcal{F}\gamma$	γ

where we used $w \gg a$ to convert a sum into an integral, $\sum_n \to (1/a^2)\int_{L_a^2} d\mathbf{r}_\perp$. Here η expresses the fraction of the spatial mode that overlaps with the atomic array of area $L_a^2 = a^2N$, and is given by an error function for the Gaussian target mode; in the limit of a large enough array, $L_a \gg w$, this overlap tends to unity, $\eta \to 1$. Using the mode normalization length a_{eff} in Eq. (28) for the coupling of the array to the target mode, we have $\Gamma = \eta\Gamma_0$, with Γ_0 from Eq. (33).

This result has the following physical interpretation: recalling that $\Gamma_0 = \Gamma_{\mathbf{k}_\perp=0}$ is the coupling of a paraxial beam to an infinite array, this coupling is reduced by the geometrical overlap η of a finite-size array. It accounts for the fact that a fraction $(1-\eta)$ of the beam extends beyond the finite-size array and hence does not interact with the atoms [see Fig. 3(b)]. This adds a collective component $\Gamma_0 - \Gamma = (1-\eta)\Gamma_0$ to the loss rate, as also seen

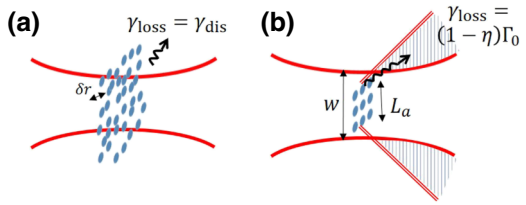

FIG. 3. Sources of imperfection and loss in an ordered atom array. (a) Disorder δr in atomic positions around the perfect lattice points leads to an effectively individual-atom scattering to undesired modes at rate $\gamma_{\rm dis}$. (b) The finite size of the array (linear size $L_a = \sqrt{N}a$) leads to its nonideal overlap with the target mode, $\eta = \mathrm{erf}^2(L_a/\sqrt{2}w) < 1$, and hence to a fraction $(1-\eta)$ of the collective emission that spills over to undesired modes. The error scalings induced by these loss mechanisms are summarized in Table II.

TABLE II. Scaling of the error $1 - r_0 = 1/(C+1) \approx 1/C$ due to different sources of imperfection and loss. The error due to position disorder [Fig. 3(a)] scales quadratically with the standard deviation δr about the perfectly ordered array positions [29,35,37]. The error due to the imperfect overlap between the target mode and the array due to the latter's finite size [Fig. 3(b)] scales essentially exponentially better with the atom number $N = L_a^2/a^2$ (asymptotic result valid for $L_a \gg w$).

Loss mechanism	Effective error	Scaling
Disorder	$1 - r_0 = \dfrac{\gamma_{\rm dis}}{\Gamma_0 + \gamma_{\rm dis}}$	$(2\pi\delta r/\lambda)^2$
Finite-size array	$1 - r_0 = 1 - \eta$	$\dfrac{2}{\sqrt{\pi}}\dfrac{\sqrt{2}w}{L_a}\exp[-L_a^2/(2w^2)]$

from Eq. (30). To conclude, we get the following mapping parameters:

$$\Gamma = \eta\Gamma_0, \quad \gamma_{\rm loss} = (1-\eta)\Gamma_0 + \gamma_s, \tag{35}$$

with Γ_0 from Eq. (33).

C. Efficiency analysis

As explained above, once the mapping to the 1D model of Eq. (6) is established, the efficiency of the light-matter interface is completely determined by the effective parameters Γ and $\gamma_{\rm loss}$ (Table I), and the resulting resonant reflectivity $r_0 = C/(C+1) = \Gamma/(\Gamma + \gamma_{\rm loss})$.

Beginning with the desired emission to the target mode, $\Gamma = \eta\Gamma_0$, it is given by the effective 1D emission rate multiplied by the overlap factor η between the array and target-mode cross sections, Eq. (34).

The undesired emission rate $\gamma_{\rm loss}$ from Eq. (35) has two contributions. The individual-atom rate $\gamma_s = \gamma_{se} + \gamma_{\rm dis}$ includes the emission rate from $|e\rangle$ to $|s\rangle$ [recalling that it may become negligible in ladder-type atoms, Fig. 1(c)] and the disorder-induced scattering. For the latter, we consider a standard deviation δr in atomic positions around the array lattice positions $\mathbf{r}_n$ in all directions x, y, z [Fig. 3(a)]. This breaks translation invariance and causes scattering to directions other than that of the target mode. To lowest order, this results in an effective individual-atom scattering rate that can be shown to scale as $\gamma_{\rm dis} \sim (2\pi\delta r/\lambda)^2\Gamma_0$ [29,35,37].

For an array comparable in size or smaller than the target beam cross section ($L_a \lesssim w$), where $\eta < 1$, the collective decay also contributes to the undesired emission rate $(1-\eta)\Gamma_0$. This can be intuitively understood from Fig. 3(b) as follows: light diffracted from the edges of the array has an angular spread of λ/L_a, which could be larger than the angular spread λ/w contained in the target mode, so a portion $(1-\eta)$ of the light emitted from the array is not emitted into the desired target mode. For a target Gaussian mode, where η is given by $\mathrm{erf}^2\left(\frac{L_a}{\sqrt{2}w}\right)$ [Eq. (34)], we obtain the first correction to the ideal $\eta = 1$ case by expanding to first order in w/L_a, obtaining $1 - \eta = \frac{2}{\sqrt{\pi}}\frac{\exp[-L_a^2/(2w^2)]}{L_a/(\sqrt{2}w)}$. For a quantum memory, this error can then scale exponentially better with the size of the array, or equivalently with the number of atoms, as was also found numerically in Refs. [27,31] (for 1D arrays, an exponential improvement was found in the context of subradiant modes [39]). It should be noted, however, that if other sources of error are taken into account, such as the dispersion of the Gaussian beam neglected here, the exponential improvement is not necessarily observed [31]. However, for sufficiently wide Gaussian beams of even a few λ, this beam dispersion becomes negligible and the exponential scaling dominates as also seen below.

D. Direct numerical verification

The scaling of the undesired rates due to both imperfections $\gamma_{\rm dis}$ and $(1-\eta)$ is summarized in Table II. Testing these analytical predictions using independent direct numerical calculations can provide the verification for the mapping to the 1D model and the operational meaning of the resulting r_0 as an efficiency for quantum tasks. To this end, we begin by using an important principle revealed in this work—namely, that r_0 can be extracted from scattering experiments when the mapping is valid. We perform classical numerical calculations of the scattering of a right-propagating Gaussian beam off an array in different configurations [29]. We scan the frequency of the incident field looking for peaks in the intensity of the back-reflected field, thus finding the on-resonance reflectivity $R = r_0^2$. If this extracted value of r_0 agrees with that obtained analytically from the mapping, i.e., $r_0 = \Gamma/(\Gamma + \gamma_{\rm loss})$ from Eq. (35) and Table II, then the mapping to the 1D model is good and r_0 should indeed quantify the efficiency of quantum tasks. The latter can also be checked,

e.g., for the quantum memory protocol, by a direct calculation of the memory error ε. This is performed by use of the numerical method described in Ref. [31], with the same array configuration and for a retrieval of a spin wave to the two-sided symmetric target mode, with the same Gaussian shape as in the scattering calculations. Here again, if the mapping is valid, we should obtain $\varepsilon = 1 - r_0$ with $r_0 = \Gamma/(\Gamma + \gamma_{\text{loss}})$ from the analytical theory. We note that both these numerical calculations do not include the contribution γ_{se} from the $|e\rangle \to |s\rangle$ transition to the individual decay γ_s: for the scattering we take two-level atoms and for the quantum memory calculation method from Ref. [31] a ladder system is assumed [Fig. 1(c)]; therefore, the only sources of loss are the noncollective emission due to the disorder $\gamma_s = \gamma_{\text{dis}}$ and the imperfect overlap of the beam with the array $(1-\eta)\Gamma_0$ from Table II.

We begin by considering the effect of a finite-size array. Figure 4(a) shows the numerical scattering calculation of $1 - r_0$ as a function of the number of atoms $N = L_a^2/a^2$ for a fixed beam waist. In this case the atoms are perfectly ordered, so the only unwanted emission rate is due to the imperfect overlap between the array and the beam, $\frac{1}{C} = \frac{(1-\eta)\Gamma_0}{\eta\Gamma_0}$. It is seen that the numerical calculation agrees very well with this analytical expression for a Gaussian beam, $\eta = \text{erf}^2\left(\frac{L_a}{\sqrt{2}w}\right)$. Exponential scaling is observed within the parameter regime of our calculations, in agreement with the approximated expression from Table II. In addition, we also plot in Fig. 4(a) the numerically calculated error ε of the quantum memory, which is also seen to agree with the analytical prediction of the 1D mapping, $1 - r_0$, and the reflectivity extracted from the scattering calculation. These results show that, at least within the realistic parameter regime considered here, the mapping of the paraxial Gaussian target mode and the nonideal 2D ordered array to the 1D model, as summarized in Eq. (35) and Tables I and II, is indeed valid, establishing the reflectivity r_0 as a figure of merit of this quantum interface.

In addition, we consider weak disorder in atomic positions for an array size sufficiently larger than the incident beam waist, so that $\eta \approx 1$ and γ_{loss} is completely dominated by the disorder, yielding $\frac{1}{C} = \frac{\gamma_{\text{dis}}}{\Gamma_0}$. The results for $1 - r_0 \approx \frac{1}{C}$ extracted from a numerical classical scattering calculation as described above are plotted in Fig. 4(b) as a function of the standard deviation of atomic positions δr. The linear fit to the log-log plot confirms the quadratic scaling predicted analytically, $\gamma_{\text{dis}} \sim (2\pi\delta r/\lambda)^2\Gamma_0$ (Table II). A similar result is also found for the error of the quantum memory evaluated numerically as described above. The slight difference between the reflectivity and memory numerical calculations is attributed to the z component of the position disorder that breaks the symmetry between right-scattered and left-scattered light and hence leads to small deviations from the symmetric 1D model. This affects the reflectivity more than the memory protocol,

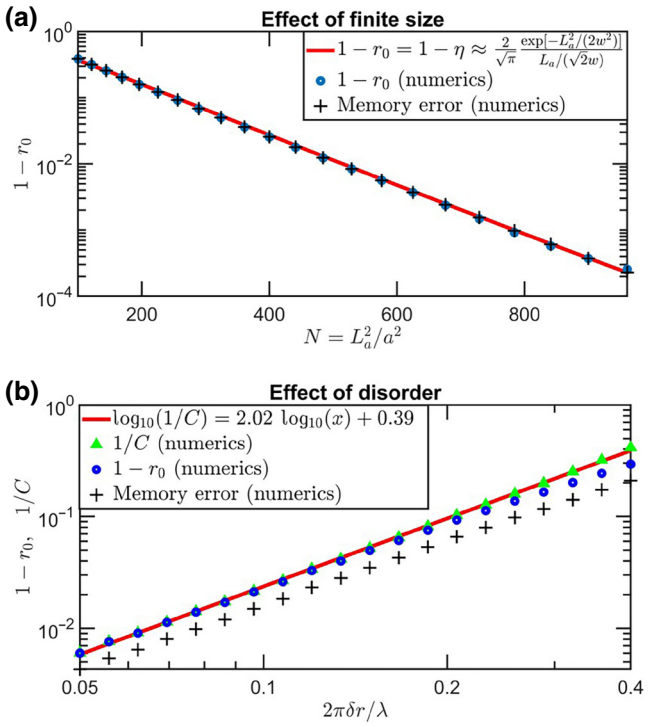

FIG. 4. Error (inefficiency) $1 - r_0$ in an ordered 2D array interface coupled to a Gaussian-beam target mode, estimated from independent numerical calculations of both the scattering (reflectivity) and quantum memory efficiency (see Sec. IV C). Agreement with the predicted analytical scaling in Table II is exhibited, in correspondence to the dominant source of imperfection. (a) Effect of finite array size: $1 - r_0$ as a function of the atom number $N = L_a^2/a^2$ for a perfectly ordered array. The error $1 - r_0$ decreases exponentially with N, as predicted analytically from the error-function behavior of the overlap η between the array and the Gaussian target mode. Here the waist and lattice spacing were fixed to $w/\lambda = 4.8$ and $a/\lambda = 0.6$, and the reflectivity was extracted from scattered fields calculated at distance $z = 5\lambda$ from the array. The corresponding quantum memory error is obtained from the calculation of the retrieval fidelity [31] with an identical initial Gaussian profile. (b) Disorder imperfection: the error $1 - r_0 = 1/(C+1) \approx 1/C$ plotted as a function of the standard deviation δr around perfect 2D array positions (averaged over 50 disorder realizations). The linear fit to the log-log plot in both the reflectivity and the memory calculations verifies the scaling $1/C = \gamma_{\text{dis}}/\Gamma_0 \sim (2\pi\delta r/\lambda)^2$ predicted analytically for a large enough array with respect to the incident-beam waist, $L_a = \sqrt{N}a > w$ (see Table II and the main text). Numerical parameters: $w/\lambda = 4.8$, $a/\lambda = 0.6$, and atom number $N = 30 \times 30$. Slight deviations between the reflectivity and memory errors arise mainly from the z component of the position disorder, which breaks the symmetry between left-scattered and right-scattered light.

recalling that in the former illumination and detection are in opposite propagation directions, whereas in the latter they are two-sided. We further verify, by considering x-y and z position disorder separately, that while both lead to

the same scaling of the losses, $\gamma_{\rm dis} \propto (\delta r)^2$, in the case of x-y disorder the losses are smaller and the difference between memory and reflection results practically disappears.

E. Beyond $a < \lambda$

Finally, we comment on the situation where the lattice spacing a may exceed the wavelength λ. In this case, even for an infinite array and plane wave illumination ($w \to \infty$), scattering of light from the collective dipole $\hat{P}$ exists in multiple diffraction orders and not only in the zeroth-order, incident field direction [29]. These additional diffraction orders lead to additional loss channels with a total emission rate $\gamma_{\rm diff}$ that is added to $\gamma_{\rm loss}$ (Table I) and that is given by [29,65]

$$\gamma_{\rm diff} = \Gamma_0 \sum_{(m_x,m_y)\in {\rm LC}, \neq (0,0)} \frac{1 - \frac{\lambda^2}{a^2}|(m_x,m_y)\cdot \mathbf{e}_d|^2}{\sqrt{1-\frac{\lambda^2}{a^2}(m_x^2+m_y^2)}}. \quad (36)$$

Here the sum is taken over all diffraction orders $(m_x, m_y) \neq (0,0)$ (with m_x and m_y integers) that are within the light cone (LC), i.e., that satisfy $|(m_x, m_y)| < a/\lambda$ and describe propagating waves.

V. EXAMPLE 2: PARTIALLY FILLED ARRAY

While the previous example focused on using the 1D model approach to provide a meaningful analytical description of a quantum interface, we now wish to use the power of this approach to greatly enhance the interface efficiency. In particular, previous work commonly assumed that the target mode is a Gaussian beam [29,31,52,53], taking advantage of its efficient coupling to an ordered array (as analyzed in detail in Sec. IV). Going beyond the lattice symmetry of an ordered array, however, our 1D model apporoach can be harnessed to achieve greatly enhanced coupling efficiencies by properly designing the target mode. The idea is that given a collection of atomic positions, the mapping to the 1D model becomes more reliable as the target photon mode is more accurately matched to a paraxial eigenmode of the dipole-dipole interaction kernel. If the atomic ensemble is also sufficiently dense, then radiation from the corresponding dipole eigenmode will also mostly couple to the target mode, yielding large efficiency.

We apply this idea to the case of a partially filled atomic array, showing that the mapping to the 1D model exists, opening up the possibility for the design of enhanced efficiency of such disordered arrays. From a practical standpoint, this possibility entails the following advantage: the stringent requirement to build arrays with a nearly perfect filling fraction (e.g., the creation of a Mott insulator [30]) is now alleviated if one can measure the atomic positions of a partially filled array; the latter allows one to calculate the eigenmodes of the dipole-dipole interaction kernel and accordingly shape the spatial profile of the incident beam (e.g., using a spatial light modulator).

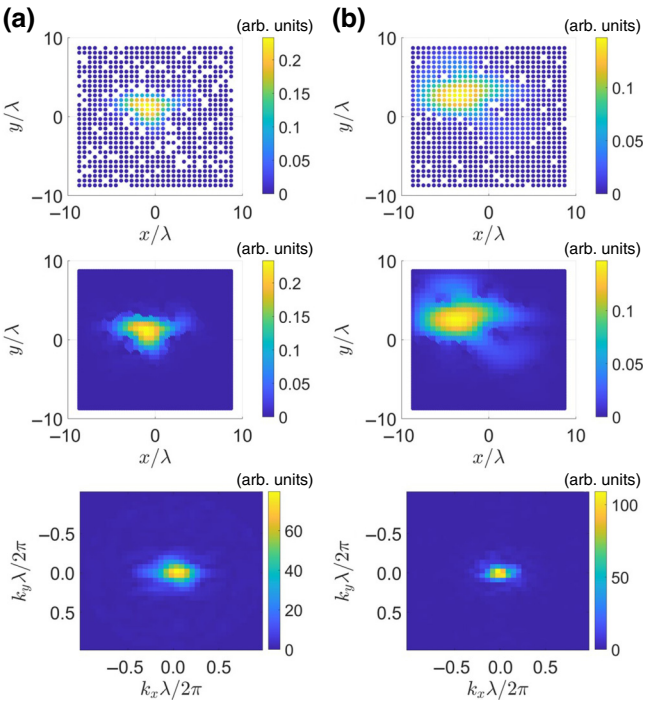

FIG. 5. Paraxial dipole eigenmodes, Eq. (21), of a realization of a partially filled 2D array with 30×30 lattice sites, lattice constant $a/\lambda = 0.6$, and filling fraction (a) 0.85 and (b) 0.95. The top panel displays the most paraxial eigenmode $v_{0,n}$ represented on the discrete array sites. The middle panel shows the corresponding continuous function $u(\mathbf{r}_\perp)$ constructed from the interpolation of the eigenmode, and chosen as the target photon mode. The Fourier transform of the mode $u(\mathbf{r}_\perp)$ is shown in the bottom panel: we note its paraxial character evident by its small bandwidth around $\mathbf{k}_\perp = (k_x, k_y) = (0,0)$.

To simulate how this works, we numerically construct partially filled arrays by randomly loading atoms into a perfect 2D lattice. Using the theory of the mapping to the 1D model, Sec. III, we then perform the following procedure on each random array realization. We generate the dipole-dipole interaction matrix $D_{nm} \propto G(\omega_p, \mathbf{r}_n^\perp - \mathbf{r}_m^\perp, 0)$ from the atomic positions $\mathbf{r}_n^\perp$, and find its eigenvectors $v_{l,n}$ and eigenvalues D_l as in Eq. (21). Using numerical interpolation, we construct from each eigenvector $v_{l,n}$ (defined on the discrete space $\mathrm{r}_n^\perp$) a corresponding continuous normalized function $u_l(\mathbf{r}_\perp)$ (defined on the continuous x-y space $\mathrm{r}_\perp$), satisfying $u_l(\mathbf{r}_\perp = \mathbf{r}_n^\perp) \propto v_{l,n}$. Then, performing a Fourier transform to $\mathbf{k}_\perp$-space for each mode $u_l(\mathbf{r}_\perp)$, we identify the most paraxial mode (denoted by $l = 0$) and choose it as our target mode $u(\mathbf{r}_\perp)$. Finally, the corresponding effective length $a_{\rm eff}$ [Eq. (20)] and eigenvalue D_0 determine our mapping parameters Γ and $\gamma_{\rm loss}$ according to Eqs. (28) and (30).

Figure 5 shows examples of the most paraxial eigenmodes of 2D arrays with filling fractions of 0.85 and 0.95.

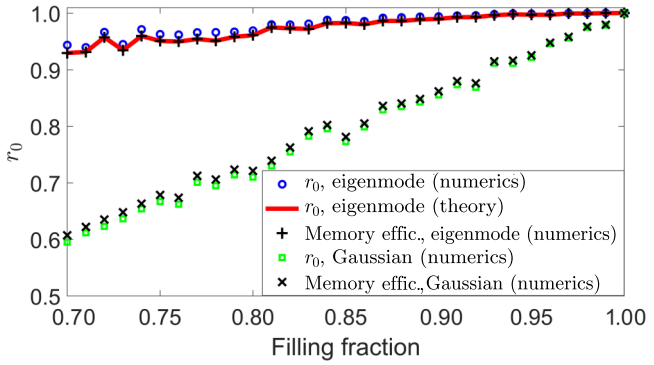

FIG. 6. Boosting the efficiency using dipole-eigenmode target modes. Efficiency (reflectivity) r_0 of a partially filled 2D array as a function of the filling fraction for a randomly filled square lattice of 30×30 sites and lattice constant $a = 0.6\lambda$ averaged over ten realizations. The theoretically expected value $r_0 = \Gamma/(\Gamma + \gamma_{\text{loss}})$ (solid red line), determined from Eqs. (28) and (30) for each realization, exhibits excellent agreement with direct numerical calculations of both the scattering reflectivity (blue circles) and the quantum memory efficiency (black crosses): in the numerical calculations the target mode is taken as the most paraxial eigenmode constructed as in Fig. 5. High efficiencies $r_0 > 0.99$ and $r_0 > 0.94$ are observed for filling fractions as low as 0.85 and 0.70, respectively. In comparison, we plot the numerically calculated reflectivity and quantum memory efficiency for a Gaussian-beam target mode (with a waist optimized to the perfectly filled array), which are seen to reach much lower values, demonstrating the superiority of the eigenmode approach suggested by the theory.

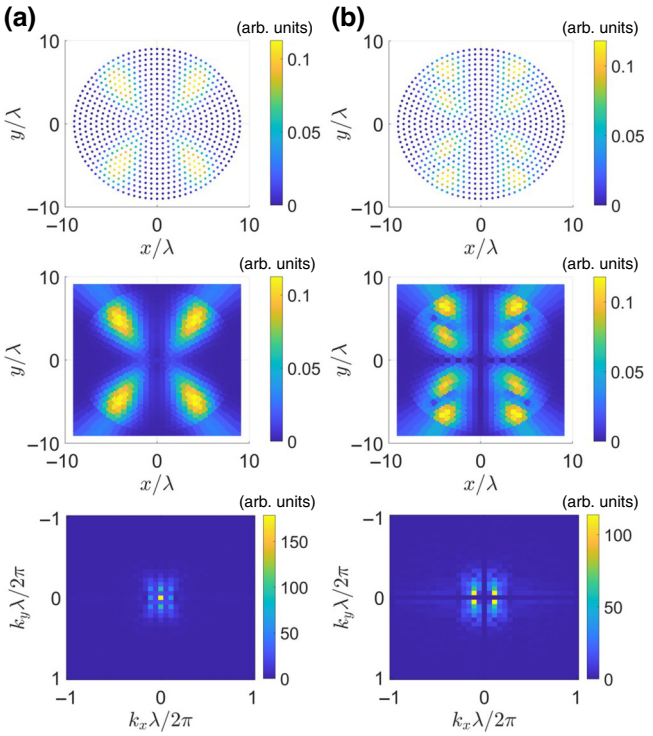

FIG. 7. Two examples (a) and (b) of paraxial eigenmodes in the circular array described in Sec. VI. The top panel presents the eigenmodes $v_{l,n}$ on the array sites, the middle panel shows the corresponding continuous functions $u_l(\mathbf{r}_\perp)$ constructed from the eigenmodes by interpolation, and the bottom panel displays the Fourier transform of these functions. The paraxial character of the modes is exhibited by their narrow bandwidth in Fourier space around $\mathbf{k}_\perp = (k_x, k_y) = (0, 0)$.

The top panel presents the eigenmodes $v_{l,n}$ on the discrete atomic sites $\mathbf{r}_n^\perp$, whereas the middle panel shows the corresponding interpolated functions $u(\mathbf{r}_\perp)$, chosen as the target modes. The paraxial character of the modes is evident by their $\mathbf{k}_\perp$-space representations (bottom panel), which are seen to be well concentrated around $\mathbf{k}_\perp = 0$. This matches their smooth spatial profiles, which avoid regions of missing atoms.

The efficiency predicted by the 1D model mapping is given by $r_0 = \Gamma/(\Gamma + \gamma_{\text{loss}})$, with Γ and γ_{loss} estimated as described in the previous paragraphs. This theoretical prediction for r_0 is plotted in Fig. 6 as a function of the filling fraction, exhibiting excellent agreement with the numerical calculations of both the reflectivity and the memory efficiency. For the latter, numerical simulations are performed as described in Sec. IV D, using the same partially filled array realizations and by shining and detecting the corresponding target modes $u(\mathbf{r}_\perp)$ from the theory [66]. We observe high efficiencies $r_0 > 0.99$ and $r_0 > 0.94$ even for filling fractions as low as 0.85 and 0.70, respectively. In contrast, when we perform the scattering (reflectivity) and quantum memory numerical simulations with the same partially filled array but using a typical Gaussian-beam target mode (whose waist is optimized for the corresponding finite-size perfect array), we observe a quick drop in the efficiency as the filling fraction is lowered. The clear superiority of the former results is a direct consequence of the design of the target mode following our 1D model approach, and should be useful in enhancing the efficiency of the quantum interface.

VI. EXAMPLE 3: CIRCULAR ARRAY

Another example that deviates from the 2D-lattice array is that of a circular array, as depicted in Fig. 7. The circular array is constructed from several rings, with a fixed distance a between the rings and a fixed distance b between the positions of the atoms on each ring. We choose $b = (2\pi/6)a$, so the spacing between atoms on the same ring is similar to the spacing between atoms on adjacent rings. Nevertheless, the system lacks the discrete translation invariance of the 2D ordered array, although it still exhibits paraxial dipole-dipole eigenmodes. Importantly, the latter means that the circular array can be mapped to the 1D model by a proper choice of the target mode, as we show in the following.

Using the same mapping procedure described in the previous section, we begin by numerically calculating the eigenmodes $v_{l,n}$ of the dipole-dipole interaction kernel D_{nm} of the array (Fig. 7, top panel), followed by constructing the corresponding continuous functions $u_l(\mathbf{r}_\perp)$, satisfying $u_l(\mathbf{r}_\perp = \mathbf{r}_n^\perp) \propto v_{l,n}$ (Fig. 7, middle panel). By examining their Fourier transforms, we choose a pair of modes $u_l(\mathbf{r}_\perp)$ that are paraxial, i.e., relatively narrow around $\mathbf{k}_\perp = 0$ (Fig. 7, bottom panel). For each such paraxial mode, we can define the mapping to the 1D model by identifying it as the target mode. We then find the mapping parameters and the corresponding efficiency r_0 predicted by the theory for each such target mode, as explained in the previous section. We perform this procedure for the two paraxial eigenmodes presented in Fig. 7, indeed finding that they both exhibit high efficiencies: i.e., $r_0 = 0.9459$ and $r_0 = 0.9242$ for the examples from Figs. 7(a) and 7(b), respectively. We also compare these theoretically predicted efficiencies with the reflectivity obtained from numerical scattering calculations using the same target modes, finding similar results: $r_0 = 0.9688$ and $r_0 = 0.9560$ for the examples from Figs. 7(a) and 7(b), respectively. The small differences are attributed to deviations from both paraxiality and the single-mode picture.

VII. EXTENSION TO MULTIPLE LAYERS

So far we have focused on planar structures where the atoms are spread along the x-y plane at $z = 0$. We now proceed to extend the formalism developed in Sec. III to include 3D structures consisting of multiple layers of identical planar structures. We show that by choosing the separation between the layers to satisfy the Bragg condition, Eq. (18), the mapping to the 1D model exists and the collective decay rates increase linearly with the number of layers. We apply this multilayer formalism to the case of a 3D ordered array.

A. System: Scattering between 2D layers

We consider N_z identical layers, with each layer consisting of $N_\perp$ atoms arranged on a plane, such that the total number of atoms N is $N_\perp \times N_z$. The atom index $n = (n_\perp, j)$ now comprises an intralayer x-y index $n_\perp = 1, \ldots, N_\perp$ and the index $j = 1, \ldots, N_z$ of different layers, with corresponding atomic operators $\hat{\sigma}_{\alpha\alpha',n_\perp j}$ at positions $\mathbf{r}_n = (\mathbf{r}_n^\perp, z_n) \to \mathbf{r}_{n_\perp j} = (\mathbf{r}_{n_\perp}^\perp, z_j)$. We define the collective dipole of a layer j in analogy to Eq. (19) of the planar, single-layer case,

$$\hat{P}_j = a_{\text{eff}} \sum_{n_\perp} u^*(\mathbf{r}_{n_\perp}^\perp) \hat{\sigma}_{ge,n_\perp j}, \tag{37}$$

and similarly for $\hat{S}_j$ with $\hat{\sigma}_{gs,n_\perp j}$. Performing this transformation on Eq. (14) for $\hat{\sigma}_{ge,n_\perp j}$ [with the replacement $(\mathbf{r}_n^\perp, z_n) \to (\mathbf{r}_{n_\perp}^\perp, z_j)$], we derive the following equation of motion for P_j (see Appendix F):

$$\frac{d\hat{P}_j}{dt} = \left[i(\delta_p - \Delta) - \frac{\gamma_s}{2} \right] \hat{P}_j - \frac{\Gamma_0}{2} \sum_{j'=1}^{N_z} e^{ik_p |z_j - z_{j'}|} \hat{P}_{j'} + i\sqrt{\Gamma_{1D}} \hat{\mathcal{E}}_{0,j} + i\Omega \hat{S}_j + \hat{F}_j. \tag{38}$$

Here we have already taken the mode profile that satisfies Eq. (23), i.e., it matches a dipole eigenmode of the planar layers with eigenvalue $D_0 = \Gamma_0/2 + i\Delta$ (recalling that all layers are identical). The input field on the layer j, given by $\hat{\mathcal{E}}_{0,j} = [\hat{\mathcal{E}}_{0,+}(z_j) + \hat{\mathcal{E}}_{0,-}(z_j)]/\sqrt{2}$, is coupled to the corresponding layer by the 1D rate Γ_{1D} from Eq. (28), and $\hat{F}_j$ is the vacuum noise from individual-decay and dissipative collective losses, in analogy to $\hat{F}$ in Eq. (29).

This equation describes the coupling between the collective dipole $\hat{P}_j$ of a layer j, with collective shift Δ and width Γ_0, to those of different layers $j' \neq j$ via the effective interlayer dipole-dipole kernel, $-(\Gamma_0/2)e^{ik_p|z_j - z_{j'}|}$. The latter is proportional to the Green's function of 1D electrodynamics, and is identical to dipole-dipole interaction familiar from 1D "waveguide" QED [59,67,68]. Within this picture, each 2D layer forms a dipole in one dimension, and these identical dipoles exhibit a collective emission $\cos(k_p|z_j - z_{j'}|)$ and frequency shift $\sin(k_p|z_j - z_{j'}|)$.

Therefore, Eq. (38) reveals a picture of multiple 1D-like scattering between the layers. This 1D electrodynamics picture is valid under the following reasonable conditions (see Appendix F for details). First, we assume that all of the layers lie within the Rayleigh ranges defined by the finite sizes of both the beam and the layers, $z_R = \pi w^2/\lambda$ and $\sim L_{xy}^2/\lambda$, respectively (L_{xy} being the linear size of a planar layer, e.g., $L_{xy} = L_a = a\sqrt{N}$ for the 2D ordered array from Sec. IV). This condition is what gives rise to the approximately diffractionless 1D propagation between the layers, $e^{ik_p|z_j - z_{j'}|}$. In addition to this far-field propagation, the layers also interact via evanescent fields, leading to an additional interaction term between the layers. However, assuming the separation between any pair of layers is larger than or on the order of a wavelength, $|z_j - z_{j'}| \gtrsim \lambda$, the contribution of these evanescent fields is negligible. In the following, we discuss how these near fields induce corrections to the collective detuning Δ in a 3D ordered array.

B. Mapping to the 1D model

We now show that by using the Bragg condition, Eq. (18), i.e., where all layers are situated at integer multiples of half a wavelength, one can map the multilayer system

to the generic two-sided model. First, we define the phase-matched collective dipole of the N_z identical layers as

$$\hat{P} = \frac{1}{\sqrt{N_z}} \sum_{j=1}^{N_z} e^{-ik_p z_j} \hat{P}_j, \tag{39}$$

and similarly for $\hat{S}$. Noting that the Bragg condition (18) implies that $e^{ik_p z_j} = e^{-ik_p z_j}$ for any j, we see that the 1D dipole-dipole term in Eq. (38) becomes $-\sqrt{N_z}(\Gamma_0/2)e^{ik_p z_j}\hat{P}$. For the input-field term, we similarly obtain $\hat{\mathcal{E}}_{0,j} \approx e^{ik_p z_j}\hat{\mathcal{E}}_0(0)$ (see Appendix F). Then, performing the transformation (39) on Eq. (38), we obtain the 1D model, Eq. (6), for $\hat{P}$ with the parameters

$$\Gamma = N_z \Gamma_{1D}, \quad \gamma_{\text{loss}} = N_z(\Gamma_0 - \Gamma_{1D}) + \gamma_s, \tag{40}$$

where Γ_{1D} and $\hat{\mathcal{E}}_0(0)$ are those from Eqs. (28) and (27), respectively, and the Langevin noise is given by $\hat{F} = \sum_j e^{-ik_p z_j}\hat{F}_j/\sqrt{N_z}$. Finally, the mapping is completed by noting that Eq. (17) with the definition of $\hat{P}$ in Eq. (39) and the Bragg condition simply yields the field equation of the two-sided model, Eq. (4).

This result shows that when the Bragg condition is satisfied, the phase-matched collective dipole diagonalizes the 1D dipole-dipole kernel in Eq. (38). Furthermore, the resulting mapping to the two-sided model exhibits collective effects that grow linearly with the number of layers N_z. For situations where collective effects do not contribute much to the loss ($\gamma_{\text{loss}} \approx \gamma_s$), the latter implies a linear growth of the cooperativity $C = \Gamma/\gamma_{\text{loss}}$ with N_z.

Conversely, when the Bragg condition is far from being satisfied, mapping to the two-sided model is impossible and a behavior similar to propagation and extinction can exist: an effective optical depth growing linearly with N_z emerges, $\text{OD} \propto N_z$, leading to exponential decay of the propagated light $e^{-\text{OD}}$, as discussed in Appendix G.

C. Example: 3D ordered atom array

As an example we consider a 3D ordered array as illustrated in Fig. 8(a). Each layer consists of a finite-size 2D array as described in Sec. IV, and the layers are positioned at $z_j = ja_z$ ($j = 1, \ldots, N_z$) with longitudinal lattice spacing a_z not necessarily equal to the lattice constant a in the x-y plane. Moreover, while a can take any value in principle, a_z has to be either an even or an odd multiple of $\lambda/2$ to conform with the Bragg condition (18) that guarantees the mapping to the two-sided 1D model. Then the collective dipole $\hat{P}$ from Eq. (39) becomes either a symmetric or an alternating-sign superposition of the layers $\hat{P}_j$, respectively.

1. Mapping to the 1D model

Applying our general results from Eq. (40) to this case, using those of an individual 2D array layer from Eq. (35),

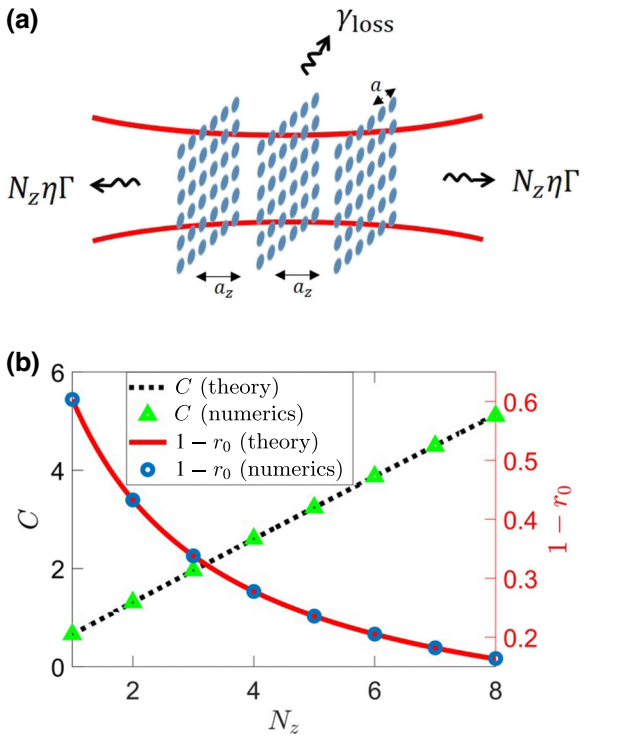

FIG. 8. (a) A 3D ordered atomic array is described as consisting of N_z layers, each being a 2D array (here $N_z = 3$). (b) Cooperativity $C = \Gamma/\gamma_{\text{loss}}$ and error $1 - r_0 = 1/(1 + C)$ versus the number of layers N_z of a phase-matched array [$a_z = (\lambda/2) \times \mathbb{N}$]. For the parameters chosen ($a/\lambda = 0.6$, $N_\perp = 30$, $a_z/\lambda = 1$, $\gamma_s = \gamma$, and $w/\lambda = 6$), the individual decay dominates the loss, $\gamma_{\text{loss}} \approx \gamma_s$, so C increases linearly with N_z (see Table I). Excellent agreement between the analytical theory [Eq. (41)] and numerical scattering calculations is exhibited.

we find the mapping parameters

$$\Gamma = N_z \eta \Gamma_0, \quad \gamma_{\text{loss}} = N_z(1-\eta)\Gamma_0 + \gamma_s, \quad \Gamma_0 = \frac{3}{4\pi}\frac{\lambda^2}{a^2}\gamma. \tag{41}$$

Here η is that from Eq. (34), i.e., it describes the spatial overlap between the target mode and the finite-size 2D array layers, and we recall it is given by $\eta \to \text{erf}^2\left(\frac{L_a}{\sqrt{2}w}\right)$ for a Gaussian target mode of waist w and with $L_a = a\sqrt{N_\perp}$.

We verify this analytical result via numerical scattering calculations as described in Sec. IV D. In Fig. 8(b), we observe excellent agreement between $1 - r_0 = \gamma_{\text{loss}}/(\Gamma + \gamma_{\text{loss}})$ obtained analytically from Eq. (41) and that extracted from the numerical calculation of the reflectivity, as a function of the number of layers N_z (and considering the same beam waist and finite-size array parameters). For a closer examination of the scaling with N_z, we plot the cooperativity $C = \Gamma/\gamma_{\text{loss}}$ extracted from the reflectivity via $r_0 = C/(C + 1)$. We observe a linear

dependence of C with N_z, reflecting the fact that we are working in the regime of individual-decay dominant losses, $\gamma_{\text{loss}} \approx \gamma_s$. To obtain this regime for a perfectly ordered array, we considered three-level atoms as in Fig. 1(b), with the decay rate to the second ground state $|s\rangle$ taken to be equal to that to $|g\rangle$, i.e., $\gamma_s = \gamma_{\text{es}} = \gamma$. In the classical numerical calculation, this situation can be simulated by considering a polarizability of a two-level atom with a "nonradiative" decay equal to γ [29].

2. Correction due to evanescent fields

While Eq. (38) describes 1D electrodynamics of scattering between the layers, the array is in fact a 3D structure composed of discrete point dipoles (atoms). The 3D character of this resulting electrodynamics is revealed by considering the field close enough to each layer, where its nonuniform, discrete structure in the x-y plane is evident by the near fields emanating from the atoms. To see this in our 3D array case, we derive Eq. (38) as described in Sec. VII A, but *without* the assumption that the 2D array layers are far enough from each other (without assuming that $a_z|j - j'| \gtrsim \lambda$). We then obtain Eq. (38) for $\hat{P}_j = (a/\sqrt{\eta}) \sum_{n_\perp} u^*(\mathbf{r}^\perp_{n_\perp}) \hat{\sigma}_{ge,n_\perp j}$, wherein the 1D dipole-dipole kernel $(\Gamma_0/2)e^{ik_p|z_j - z_{j'}|}$ is replaced by the target-mode projected dipole-dipole kernel (see Appendix H)

$$\mathcal{D}_{jj'} = \frac{\Gamma_0}{2} \sum_{m_x=-\infty}^{\infty} \sum_{m_y=-\infty}^{\infty} \frac{1 - \frac{\lambda^2}{a^2}|(m_x, m_y) \cdot \mathbf{e}_d|^2}{\sqrt{1 - \frac{\lambda^2}{a^2}(m_x^2 + m_y^2)}} \times e^{ik_p \sqrt{1 - \frac{\lambda^2}{a^2}(m_x^2 + m_y^2)} a_z |j - j'|}. \tag{42}$$

The sum over (m_x, m_y) accounts for contributions from the diffraction orders of each 2D layer. It is seen that every diffraction order (m_x, m_y) mediates a quasi-1D interaction between the layers, $\propto e^{ik_z^{m_x,m_y} a_z |j - j'|}$, with $k_z^{m_x,m_y} = k_p \sqrt{1 - (\lambda^2/a^2)(m_x^2 + m_y^2)}$. The latter represents both one-dimensionally-propagating or evanescent waves ($k_z^{m_x,m_y}$ being real or imaginary, respectively), depending on the lattice spacing a/λ and the diffraction order (m_x, m_y), similarly to the interaction mediated by a multimode waveguide [67]. Considering a subwavelength array, $a < \lambda$, only $(m_x, m_y) = (0, 0)$ can propagate, giving

$$\mathcal{D}_{jj'} = \frac{\Gamma_0}{2} e^{ik_p a_z |j - j'|} + i\varepsilon_{jj'}, \tag{43}$$

with

$$\varepsilon_{jj'} = \frac{\Gamma_0}{2} \sum_{(m_x,m_y) \neq (0,0)} \frac{\frac{\lambda^2}{a^2}|(m_x, m_y) \cdot \mathbf{e}_d|^2 - 1}{\sqrt{\frac{\lambda^2}{a^2}(m_x^2 + m_y^2) - 1}} \times e^{-k_p a_z |j - j'| \sqrt{\frac{\lambda^2}{a^2}(m_x^2 + m_y^2) - 1}}. \tag{44}$$

This term is a deviation from the purely 1D picture, as it describes the interaction via the evanescent waves of higher diffraction orders. Their evanescent character dictates an exponentially decaying interaction at a range of $\xi_{m_x,m_y} = a/(2\pi\sqrt{m_x^2 + m_y^2 - (a/\lambda)^2})$, which becomes shorter for increasing orders m_x, m_y and with a typical length scale a. Assuming an interlayer distance $a_z \gtrsim \xi_{1,0}$, we can thus treat the term $\varepsilon_{j,j'}$ as a perturbation. Within lowest-order perturbation theory, its effect can be estimated as the matrix element between the collective dipole mode, $\Delta' = \frac{1}{N_z} \sum_{j=0}^{N_z} \sum_{j \neq j'}^{N_z} \varepsilon_{jj'} e^{ik_p a_z (j - j')}$. Accounting for the evanescent fields in this way then still allows for the mapping to the 1D model, however with the collective energy shift Δ of $\hat{P}$ now supplemented by the above correction Δ'. This is indeed verified in Appendix H for the regime under study.

VIII. DISCUSSION: UNIVERSAL APPROACH

This work introduces an approach for analyzing two-sided quantum light-matter interfaces by putting forward the universal role of the reflectivity. The approach roughly consists of two complementary parts: (1) Introducing a minimal 1D scattering model of a two-sided quantum interface that is characterized by a reflectivity r_0. Within the model we found that the efficiencies of quantum tasks are given by r_0. (2) Development of the mapping procedure collective atom-array interfaces onto the 1D model, including general results for the efficiency r_0 and the way to enhance it.

Going forward, this approach opens the prospect for a unified treatment of more applications and platforms. First, consider quantum protocols and tasks beyond those discussed here; say, the generation of photonic 1D cluster states via an array [50]. Then, instead of estimating the result of an application of the protocol on the full atom-array system, the idea promoted here is to implement it on the simple 1D model (or its suitable variant). The result, in terms of r_0, can then be related to the required atom-array system via the mapping from Eqs. (28) and (30) (or from Tables I and II, in the specific case of ordered atomic arrays and a Gaussian target mode).

Second, consider that one is interested in atom-array interfaces beyond the examples covered in this paper. As demonstrated here, for any atomic structure, one can first verify if the mapping conditions are met (i.e., the existence of a paraxial dipole eigenmode, in addition to the Bragg condition of a multilayer structure). When the conditions are met, the efficiency r_0 is simply extracted by a measurement or a classical calculation of the reflectivity. For interfaces that do not exactly conform to the mapping conditions specified in this paper, it will be interesting to develop, along similar lines, an alternative approach for a mapping to a generalized, yet simple model of an interface.

ACKNOWLEDGMENTS

We acknowledge fruitful discussions with Nir Davidson, Ofer Firstenberg, Darrick Chang, and Inbar Shani and financial support from the Israel Science Foundation (Grant No. 2258/20), the Israel Science Foundation and the Directorate for Defense Research and Development (Grant No. 3491/21), the Center for New Scientists at the Weizmann Institute of Science, the Council for Higher Education (Israel), and QUANTERA (PACE-IN). This research was made possible in part by the historic generosity of the Harold Perlman family.

APPENDIX A: REFLECTIVITY AS AN EFFICIENCY

Here we provide details on the classical treatment of the 1D scattering problem in Sec. II, highlighting the role of the resonant reflectivity r_0 as the efficiency of radiation and absorption. Considering first the radiation from an initially excited dipole in the absence of incident fields, we solve classically Eq. (1) for the atomic dipole P, with the initial conditions $P(0) = 1$ and $\mathcal{E}_0 = 0$ (ignoring vacuum noise in the classical regime), finding

$$P(t) = e^{[i(\delta_p-\Delta)-\frac{\Gamma+\gamma_{\rm loss}}{2}]t}. \tag{A1}$$

Inserting this in the equation for the output target field, we obtain

$$\mathcal{E} = i\sqrt{\Gamma}e^{[i(\delta_p-\Delta)-\frac{\Gamma+\gamma_{\rm loss}}{2}]t}. \tag{A2}$$

The fraction of energy that is emitted to the target mode is then

$$\int_0^\infty |\mathcal{E}|^2 dt = \frac{\Gamma}{\Gamma+\gamma_{\rm loss}} = \frac{C}{1+C} = r_0. \tag{A3}$$

That is, we proved that the radiation efficiency from the dipole to the desired target mode is given by the on-resonance reflectivity $|r(\delta_p = \Delta)| = r_0$.

Next, we turn to the absorption problem, considering a cw illumination in the target mode and calculating the fraction of power absorbed by the dipole P in the steady state. We notice that the interaction term in the dynamical equation (1) for P can be derived from an effective interaction Hamiltonian $H = -\hbar\sqrt{\Gamma}\mathcal{E}_0 P^\dagger + \text{H.c.}$ This has the form of a force $f = \hbar\sqrt{\Gamma}\mathcal{E}_0$ at a frequency ω_p acting on a dipole "coordinate" P. From linear response theory [69], the power dissipated on the dipole is given by $W = \frac{1}{2}\omega_p \text{Im}[\chi(\omega_p)]|f|^2$, where χ is the susceptibility of the system defined by $P = \chi f = \chi\hbar\sqrt{\Gamma}\mathcal{E}_0$. To find χ, we solve classically the equation for P in the steady state,

$$P = \frac{1}{\frac{\Gamma+\gamma_{\rm loss}}{2} - i(\delta_p-\Delta)} i\sqrt{\Gamma}\mathcal{E}_0, \tag{A4}$$

identifying χ as

$$\chi = \frac{i/\hbar}{\frac{\Gamma+\gamma_{\rm loss}}{2} - i(\delta_p-\Delta)}. \tag{A5}$$

Therefore, on resonance $\delta_p = \Delta$, the energy absorbed by the system is given by

$$W = \frac{\omega_p}{\hbar}\frac{1}{\Gamma+\gamma_{\rm loss}}|\hbar\sqrt{\Gamma}\mathcal{E}_0|^2 = \frac{\Gamma}{\Gamma+\gamma_{\rm loss}}\hbar\omega_p|\mathcal{E}_0|^2. \tag{A6}$$

Since the input power is $\hbar\omega_p|\mathcal{E}_0|^2$, we find that the absorption efficiency, which is the ratio between the absorbed power and the input power, is given by

$$\frac{\Gamma}{\Gamma+\gamma_{\rm loss}} = \frac{C}{1+C} = r_0, \tag{A7}$$

again given by the resonant reflectivity.

Finally, to show that r_0 indeed describes the on-resonance reflectivity, we turn to the two-sided model from Eq. (4) and solve it classically for a cw input field, $\mathcal{E}_{0,\pm}(z) = \mathcal{E}_{0,\pm}(0)e^{\pm ik_p z}$. Solving for P in the steady state, and inserting the solution into Eq. (4) for the field, we find, for example, for the right-propagating component (for $z > 0$)

$$\mathcal{E}_+(z)e^{-ik_p z} = (1+r)\mathcal{E}_{0,+}(0) + r\mathcal{E}_{0,-}(0), \tag{A8}$$

with $r = r(\delta_p)$ from Eq. (5). That is, the left-going field is reflected with amplitude r and the right-going field is transmitted with amplitude $1 + r$, as in a 1D problem with reflectivity r, which becomes r_0 at resonance $\delta_p = \Delta$.

APPENDIX B: QUANTUM MEMORY PROTOCOL AND EFFICIENCY

In this appendix we discuss the quantum memory protocol for optimizing the memory efficiency in a general 1D model. We follow Ref. [16], where this problem was solved for an effectively equivalent problem of atoms in a cavity, and we show how by controlling the temporal pulse shape of the coupling field the storage and retrieval efficiencies can be optimized to $r_0 = \frac{C}{1+C}$.

We assume that all atoms initially populate the ground state. We define the storage efficiency e_s (retrieval efficiency e_r) of a photon pulse of length T (T_r) as the ratio between the number of stored excitations (retrieved

photons) and the number of incoming photons (stored excitations)

$$e_s = \frac{\langle \hat{S}^\dagger(T)\hat{S}(T)\rangle}{\int_0^T \langle \hat{\mathcal{E}}_0^\dagger \hat{\mathcal{E}}_0\rangle dt}, \quad e_r = \frac{\int_{t_0}^{t_0+T_r}\langle \hat{\mathcal{E}}^\dagger \hat{\mathcal{E}}\rangle dt}{\langle \hat{S}^\dagger(t_0)\hat{S}(t_0)\rangle}, \tag{B1}$$

so the total efficiency of the whole process, storage plus retrieval, is given by $e_{\text{total}} = e_s e_r$.

Beginning with the storage problem, we first define the input pulse shape $h_0(t)$, which is nonzero at $[0, T]$, and is normalized according to $\int_0^T |h_0(t)|^2 dt = 1$. To define $h_0(t)$, we introduce a complete, orthonormal set of functions $\{h_p(t)\}$ that satisfy $\int_0^\infty dt h_p^*(t)h_{p'}(t) = \delta_{p,p'}$ and $\sum_p h_p^*(t)h_p(t') = \delta(t-t')$, and corresponding photon-mode-lowering operators $\hat{a}_p = \int_0^\infty dt \hat{\mathcal{E}}_0(t)h_p^*(t)$, such that the quantum field can be written as $\hat{\mathcal{E}}_0(t) = \sum_p h_p(t)\hat{a}_p$. By adiabatically eliminating $\hat{P}$ from Eq. (6), we obtain the dynamical equation for $\hat{S}$,

$$\frac{d\hat{S}}{dt} = \left[i(\delta_2 - \Delta_s) - \frac{\Gamma_S + \gamma_{\text{loss}}^S}{2}\right]\hat{S} + \left[i\sqrt{\Gamma_S}\hat{\mathcal{E}}_0(0,t) + \hat{F}_S(t)\right]e^{i\varphi}, \tag{B2}$$

with $\hat{F}_S = \sqrt{\gamma_{\text{loss}}^S/\gamma_{\text{loss}}}\hat{F}$ and

$$\{\Gamma_S(t), \gamma_{\text{loss}}^S(t), \Delta_s(t)\} = \rho(t) \times \{\Gamma, \gamma_{\text{loss}}, \delta_p - \Delta\},$$
$$\sqrt{\rho}e^{i\varphi} = \frac{-i\Omega^*(t)}{(\Gamma + \gamma_{\text{loss}})/2 - i(\delta_p - \Delta)}. \tag{B3}$$

In Eq. (7) we dropped the unimportant phase φ to simplify the presentation. Assuming that we have incident light only in the pulse mode $h_0(t)$, we solve the equation for $\hat{S}$, obtaining

$$e_s = \frac{C}{1+C}\left|\int_0^T h_0(t)f(t)dt\right|^2, \tag{B4}$$

with

$$f(t) = -\frac{\frac{\Gamma_S+\gamma_{\text{loss}}^S}{2} + i\Delta_S}{\Omega(t)}\sqrt{\gamma_{\text{loss}}(1+C)} \times e^{-\int_t^T d\tau\left(\frac{\Gamma_S+\gamma_{\text{loss}}^S}{2} + i(\Delta_S - \delta_2)\right)}. \tag{B5}$$

We note that $\int_0^T |f(t)|^2 dt \le 1$, with the equality achieved under the condition $\int_0^T \Gamma_S dt \gg 1$. Therefore, when this condition is fulfilled, $\left|\int_0^T h_0(t)f(t)dt\right|^2$ can be seen to be a scalar product between normalized eigenfunctions $h_0(t)$ and $f(t)$, so $e_s \le \frac{C}{1+C}$, with the equality achieved when $f(t) = h_0^*(t)$. Extracting $\Omega(t)$ from $f(t) = h_0^*(t)$, we thus get the following dependence of the coupling field pulse shape on the quantum field pulse shape:

$$\Omega(t) = \frac{-\frac{\gamma_{\text{loss}}+\Gamma}{2} - i(\Delta - \delta_p)}{\sqrt{\gamma_{\text{loss}} + \Gamma}} \times \frac{h_0(t)}{\left(\sqrt{\int_0^t |h_0(\tau)|^2 d\tau}\right)^{\left(1+i2\frac{\Delta-\delta_p}{\gamma_{\text{loss}}+\Gamma}\right)}} e^{i\delta_2(T-t)}. \tag{B6}$$

This is the control pulse shape that maximizes the storage efficiency of the pulse $h_0(t)$, giving $e_s = \frac{C}{1+C} = r_0$.

To calculate the retrieval efficiency, we similarly define the output pulse shape that we want to retrieve, $h_r(t)$ being nonzero at $[t_0, t_0 + T_r]$ and normalized according to $\int_{t_0}^{t_0+T_r} |h_r(t)|^2 dt = 1$. Then, by solving again the dynamical equation, but now with the initial condition $\langle \hat{S}(t_0)\rangle \neq 0$ and with an input field that contains only the vacuum, we find that the optimal retrieval is given by

$$e_r = \frac{C}{1+C}\left(1 - e^{-\int_{t_0}^{t_0+T_r}(\Gamma_S + \gamma_{\text{loss}}^S)d\tau}\right). \tag{B7}$$

Again, if $\int_{t_0}^{t_0+T_r}[\Gamma_S(\tau) + \gamma_{\text{loss}}^S(\tau)]d\tau \gg 1$, the retrieval efficiency will be maximized up to $e_r = \frac{C}{1+C} = r_0$. As with the calculation performed for the storage process, we can determine the control pulse shape that will maximize the retrieval efficiency. We obtain the (conjugate) time-reverse expression as in Eq. (B6). That is, the optimal control that retrieves the photons into a mode $h_r(t)$ is just the (conjugate) time reverse of the control needed to optimally store an input pulse with a reversed time shape. The reason is that the storage and retrieval are reversed symmetric processes of each other [16].

APPENDIX C: NONLINEAR 1D MODEL

Here we elaborate on the calculation of quantum squeezing in the nonlinear model of Eq. (8), and on typical realizations of the model.

1. Quantum squeezing correlations in the weakly nonlinear regime

The Heisenberg-Langevin equation (8) can be associated with the open-system dynamics of a boson mode $\hat{P}$ affected by a non-Hermitian Hamiltonian,

$$\hat{H}_{\text{NH}} = \left(-\delta' - i\frac{\gamma'}{2}\right)\hat{P}^\dagger\hat{P} + \left(i\Omega^*\hat{P} - i\Omega\hat{P}^\dagger\right) + \frac{V}{2}\hat{P}^\dagger\hat{P}^\dagger\hat{P}\hat{P},$$
$$\Omega = -i\sqrt{\Gamma}\langle\hat{\mathcal{E}}_0(0,t)\rangle = \sqrt{\Gamma}\mathcal{E}, \quad \delta' = \delta_p - \Delta,$$
$$\gamma' = \Gamma + \gamma_{\text{loss}}, \tag{C1}$$

and corresponding quantum jumps. For weak enough excitation, $|\Omega| \ll \gamma'$, quantum jump events can be ignored (for times $t \ll \gamma'/|\Omega|^2$) and the dynamics are approximately governed by the above non-Hermitian Hamiltonian $\hat{H}_{\rm NH}$. Consistent with the weak-excitation limit, we can write a general state of the bosonic system $\hat{P}$ as an expansion in its number-state basis up to two excitations, $|\psi\rangle = c_0|0\rangle + c_1|1\rangle + c_2|2\rangle$. Assuming that the atoms are initially in their ground state, $c_0(t=0) = 1$, we solve the Schrödinger equation for the steady state of $|\psi\rangle$ under the Hamiltonian $\hat{H}_{\rm NH}$ perturbatively in $|\Omega|/\gamma' \ll 1$, finding

$$c_0 \approx 1 - \frac{|\Omega|^2}{\delta'^2 + (\gamma'/2)^2}, \quad c_1 \approx \frac{\Omega}{i\delta' - \gamma'/2}, \quad c_2 \approx \frac{\sqrt{2}\Omega^2}{(i\delta' - \gamma'/2)(i2\delta' - iV - \gamma')}. \tag{C2}$$

The squeezing parameter of a bosonic mode $\hat{P}$ satisfying $[\hat{P}, \hat{P}^\dagger]$ (as in the linearized collective dipole we consider) is defined by

$$\xi_P^2 = \min_\theta \mathrm{var}[\hat{P}e^{-i\theta} + \hat{P}^\dagger e^{i\theta}] = 1 + 2\left(\langle \hat{P}^\dagger \hat{P}\rangle - |\langle \hat{P}\rangle|^2 - |\langle \hat{P}^2\rangle - \langle \hat{P}\rangle^2|\right), \tag{C3}$$

At the steady state, we perform the averages with the state $|\psi\rangle$ and its coefficients from Eq. (C2), using the operator $\hat{P}$ at $t = 0$ (in the Schrödinger picture), obtaining, up to second order in Ω,

$$\xi_P^2 = 1 - \frac{|\Omega|^2}{4(\gamma'/2)^2 + \delta'^2} f(V) \to 1 - r_0 \frac{|\overline{\mathcal{E}}|^2}{\Gamma + \gamma_{\rm loss}} f(V), \tag{C4}$$

with $f(V) = 8\left|\frac{v}{1+v}\right|^2$ and $v = \frac{-iV/2}{-\gamma' + i\delta'}$. Here the arrow signifies the result on resonance $\delta' = 0$ ($\delta_p = \Delta$), which is given in the main text. Since $\xi_p^2 < 1$ implies quantum correlations, their strength is quantified by the second term, which is proportional to the incoming photon rate $|\overline{\mathcal{E}}|^2$ multiplied by its conversion efficiency to atomic excitations, given by r_0. It turns out that the bosonic squeezing calculated here for the approximate boson mode $\hat{P}$ is equal to the spin-squeezing parameter of the collection of two-level atoms that constitute $\hat{P}$: the generalization of spin squeezing to a nonuniform superposition of two-level atoms [in $\hat{P}$ with couplings proportional to the mode $u(\mathbf{r}_n)$ for an atom n] is discussed in, for example, Ref. [70], whereas its approximation as that of bosonic squeezing is valid in the linearized, weak-excitation limit as discussed here.

Turning to the output field, $\hat{\mathcal{E}}(z)$, the squeezing is defined in Eq. (C3), however with the normalization of the vacuum noise $[\hat{\mathcal{E}}(z,t), \hat{\mathcal{E}}^\dagger(z,t)] = [\hat{\mathcal{E}}_0(0,t), \hat{\mathcal{E}}^\dagger(0,t)] = \delta(t=0) \equiv \mathcal{V}_0$,

$$\xi_E^2 = \min_\theta \mathrm{var}[\hat{\mathcal{E}}(z)e^{-i\theta} + \hat{\mathcal{E}}(z)^\dagger e^{i\theta}]/\mathcal{V}_0 = 1 + \frac{2}{\mathcal{V}_0}\left(\langle \hat{\mathcal{E}}^\dagger \hat{\mathcal{E}}\rangle - |\langle \hat{\mathcal{E}}\rangle|^2 - |\langle \hat{\mathcal{E}}^2\rangle - \langle \hat{\mathcal{E}}\rangle^2|\right). \tag{C5}$$

We calculate the required correlators using the expression in Eq. (1) that relates $\hat{\mathcal{E}}(z)$ to $\hat{P}$ and the correlators of $\hat{P}$ found above, yielding

$$\xi_E^2 = 1 - \frac{\Gamma}{\mathcal{V}_0} \frac{|\Omega|^2}{4(\gamma'/2)^2 + \delta'^2} f(V) \to 1 - r_0^2 \frac{|\overline{\mathcal{E}}|^2}{\mathcal{V}_0} f(V), \tag{C6}$$

as given in the main text.

2. Mapping of collective systems to the 1D nonlinear model

We discuss two typical situations wherein nonlinearities in a collective atomic system exist and their mapping to the 1D nonlinear model of Eq. (8) is possible.

a. All-to-all pairwise interaction potential

Consider the general collective system from Sec. III A for two-level atoms (i.e., where the control field vanishes, $\Omega = 0$, so the third level $|s\rangle$ is irrelevant). Within the linearized regime wherein $\hat{\sigma}_{ge,n}$ is taken as a local bosonic lowering operator, we add nonlinearity by considering long-range interaction $V_{nm} = V(\mathbf{r}_n - \mathbf{r}_m)$ between pairs of atoms n and m occupying the excited state $|e\rangle$. Realistically, this can be achieved by the method of Rydberg dressing where the excited states $|e\rangle$ are weakly and off-resonantly coupled to Rydberg states that exhibit strong interatomic van der Waals interactions [18,19]. This will add an interaction term to the atomic Hamiltonian $\hat{H}_s$ in Eq. (10) of the form $\hat{V} = (1/2)\sum_n \sum_m V_{nm}\hat{\sigma}^\dagger_{ge,n}\hat{\sigma}_{ge,n}\hat{\sigma}^\dagger_{ge,m}\hat{\sigma}_{ge,m}$. The Rydberg-dressing potential $V_{nm} = V(\mathbf{r}_n - \mathbf{r}_m)$ is approximately constant within a typical range R_c that can extend to a few microns [18,19], and we assume for simplicity that all atoms in a layer are within this range, $|\mathbf{r}_n - \mathbf{r}_m| \lesssim R_c$, so $V_{nm} \approx \mathrm{const} \equiv V$. For a planar system, we recall the eigenmodes of the dipole-dipole kernel from Eq. (21) and define the corresponding collective-dipole operators

$$\hat{P}_l \equiv \sum_n v_{l,n}\hat{\sigma}_{ge,n} \;\Rightarrow\; \hat{\sigma}_{ge,n} = \sum_l v_{l,n}\hat{P}_l. \tag{C7}$$

Using the orthogonality of the modes $v_{l,n}$ as specified below Eq. (21) and taking the mode $l = 0$ that matches the target photon mode to be real as before ($v_{0,n} = v^*_{0,n}$), we

obtain the interaction term as $\hat{V} = (V/2)(\sum_n \hat{\sigma}^\dagger_{ge,n}\hat{\sigma}_{ge,n})^2 = (V/2)(\hat{P}^\dagger\hat{P} + \sum_{l\neq 0}\sum_{l'\neq 0}\hat{P}^\dagger_l\hat{P}_{l'}\sum_n v^*_{l,n}v_{l',n})^2$, recalling the notation $\hat{P} = \hat{P}_{l=0}$. Since all modes are initially unpopulated and the light from the target mode excites the mode $l = 0$, the second term with the double sum over $l, l' \neq 0$ modes effectively vanishes. The first term can be organized to give the term $(V/2)\hat{P}^\dagger\hat{P}^\dagger\hat{P}\hat{P}$ (with an additional negligible energy correction term proportional to $\hat{P}^\dagger\hat{P}$), which in turn gives rise to the required nonlinear term $-iV\hat{P}^\dagger\hat{P}\hat{P}$ in Eq. (8), thus realizing the 1D nonlinear model.

b. Bare nonlinearity of a two-level-atom array

Considering again a collection of two-level atoms as in Sec. III A for $\Omega = 0$, we now wish to account for the nonlinearity caused by the two-level nature of the atoms. Our starting point is the Heisenberg-Langevin equation for the atoms (e.g., in a planar ensemble, $z_n = 0$ for simplicity),

$$\frac{d\hat{\sigma}_{ge,n}}{dt} = -\left(\frac{\gamma_s}{2} - i\delta_p\right)\hat{\sigma}_{ge,n} + \left(-1 + 2\hat{\sigma}^\dagger_{ge,n}\hat{\sigma}_{ge,n}\right) \times \left(\frac{id}{-\hbar}\hat{E}_0(\mathbf{r}^\perp_n) - \hat{F}_n + \sum_m D_{nm}\hat{\sigma}_{ge,m}\right), \quad \text{(C8)}$$

where we recall the dipole-dipole kernel $D_{nm} \equiv -(i/\hbar)(d^2\omega_p^2/\epsilon_0 c^2)G(\omega_p, \mathbf{r}^\perp_n - \mathbf{r}^\perp_m, 0)$. This equation is equivalent to Eq. (14) in Sec. III A (with $\Omega = 0$), however, without our performing linearization, as manifested by the factor $\hat{\sigma}_{z,n} \equiv -1 + 2\hat{\sigma}^\dagger_{ge,n}\hat{\sigma}_{ge,n}$, which is taken to be -1 in the linear regime.

Performing the transformation (C7) to collective dipole operators corresponding to the eigenmodes of D_{nm}, and using the techniques and definitions from Sec. III E, we find Eq. (C8) becomes

$$\frac{d\hat{P}_l}{dt} = \left(i\delta_p - \frac{\gamma_s}{2} - D_l\right)\hat{P}_l + \hat{F}_l + i\sqrt{\Gamma}\hat{\mathcal{E}}_0(0)\delta_{l,0} - 2\sum_{l'}\sum_{l''}\hat{P}^\dagger_{l'}\hat{P}_{l''}\left[\sum_n v_{l,n}v_{l',n}v_{l'',n}\left(\frac{id}{\hbar}\hat{E}_0(\mathbf{r}^\perp_n) + \hat{F}_n\right)\right] + 2\sum_{l'}\sum_{l''}\sum_{l'''}\hat{P}^\dagger_{l'}\hat{P}_{l''}\hat{P}_{l'''}\left(\sum_n v_{l,n}v_{l',n}v_{l'',n}v_{l''',n}\right). \quad \text{(C9)}$$

As before, here we assumed that the target mode profile corresponds to a specific dipole eigenmode $l = 0$, $u(\mathbf{r}^\perp_n) = v_{0,n}/a_{\text{eff}}$, as manifested by the Kronecker $\delta\ \delta_{l,0}$ multiplying the target-mode, input-field term $\hat{\mathcal{E}}_0(0)$. The second and third lines describe the coupling between different eigenmodes l caused by the nonlinearity.

We now consider that input photons exist only in the target mode, whereas all other modes are in the vacuum, so $\hat{F}_l$ is a vacuum field and $\hat{\mathcal{E}}_0(0)$ contains photons. Assuming weak-field excitation, we then treat $\hat{\mathcal{E}}_0(0)$ perturbatively and expand Eq. (C9) up to third order in $\hat{\mathcal{E}}_0(0)$ [noting, for example, that all $\hat{P}_{l\neq 0}$ are at most of third order in $\hat{\mathcal{E}}_0(0)$], finding the equation for $\hat{P} = \hat{P}_{l=0}$

$$\frac{d\hat{P}}{dt} = i(\delta_p - \Delta)\hat{P} - \frac{\gamma_s + \Gamma_0}{2}\hat{P} + \left(i\sqrt{\Gamma}\hat{\mathcal{E}}_0(0) + \hat{F}\right) + i2\Delta\left(\sum_n v^4_{0,n}\right)(\hat{P}^\dagger\hat{P})\hat{P} + \Gamma_0\left(\sum_n v^4_{0,n}\right)(\hat{P}^\dagger\hat{P})\hat{P} + 2(\hat{P}^\dagger\hat{P})\left[\sum_n v^3_{0,n}\left(\frac{id}{\hbar}\hat{E}_0(\mathbf{r}^\perp_n) + \hat{F}_n\right)\right], \quad \text{(C10)}$$

where we recall the notation $D_0 = \Gamma_0/2 + i\Delta$. The first line describes the linear terms, with the first term including the dispersive, Hamiltonian shift Δ, and the other two terms describing dissipation and corresponding input fields (or noise), respectively. The second and third lines describe the three analogous nonlinear terms with an additional factor of order $\hat{P}^\dagger\hat{P}$ that is taken to be small in the perturbative, weak-excitation regime considered here. The first term, of order proportional to $\Delta\hat{P}^\dagger\hat{P}\hat{P}$, gives rise to a Kerr-like nonlinear potential as in the 1D nonlinear model. The second, dissipative term, proportional to $\Gamma_0\hat{P}^\dagger\hat{P}\hat{P}$, can become negligible with respect to the first term if we assume that $\Delta \gg \Gamma_0$, which is the case, for example, in dense enough arrays (due to the dominant $1/r^3$ scaling of the near-field dispersive part of dipole-dipole interaction compared with the $1/r$ scaling of the dissipative radiation part [29]. When the dissipative term is negligible, its corresponding input-field term [the last term in Eq. (C10)] must also be ignored. To conclude, assuming that $\Delta \gg \Gamma_0$ and that the last two terms in Eq. (C10) are ignored and by identification of $V = -\Delta\sum_n v^4_{0,n}$, Eq. (C10) is directly mapped to the 1D nonlinear model from Eq. (8) [we recall that $\gamma_{\text{loss}} = (\Gamma_0 - \Gamma) + \gamma_s$, Eq. (30)].

APPENDIX D: MAPPING THE COLLECTIVE SYSTEM TO THE 1D MODEL

Here we provide details on the mapping of the dynamical equations of the collective system to the 1D model.

1. The input-output relation Eq. (17)

Performing the projection (16) on the field equation (13), we have

$$\hat{E}_u(z) = \hat{E}_{u,0}(z) + \frac{1}{\sqrt{A_u}}\frac{\omega_p^2 d}{\epsilon_0 c^2}\sum_n \hat{\sigma}_{ge,n} \times \int_{-\infty}^{\infty} G(\omega_p, \mathbf{r}_\perp - \mathbf{r}^\perp_n, z - z_n)u^*(\mathbf{r}_\perp)d\mathbf{r}_\perp. \quad \text{(D1)}$$

Writing the Green's function as an in-plane momentum expansion [29], we have

$$G(\omega_p, \mathbf{r}_\perp - \mathbf{r}_n^\perp, z - z_n) = \\ = \frac{i}{8\pi^2}\int_{-\infty}^{\infty} d\mathbf{k}_\perp \left(1 - \frac{|\mathbf{k}_\perp \cdot \mathbf{e}_d|^2}{k_p^2}\right) e^{i\mathbf{k}_\perp \cdot \left(\mathbf{r}_\perp - \mathbf{r}_n^\perp\right)} \frac{e^{ik_z|z-z_n|}}{k_z}, \tag{D2}$$

with $k_p = 2\pi/\lambda$ and $k_z = \sqrt{k_p^2 - |\mathbf{k}_\perp|^2}$. Inserting this into Eq. (D1), we obtain

$$\hat{E}_u(z) = \hat{E}_{u,0}(z) + \frac{1}{\sqrt{A_u}} \frac{i}{4\pi} \frac{\omega_p^2 d}{\epsilon_0 c^2} \sum_n \hat{\sigma}_{ge,n} \\ \times \int_{-\infty}^{\infty} d\mathbf{k}_\perp \left(1 - \frac{|\mathbf{k}_\perp \cdot \mathbf{e}_d|^2}{k_p^2}\right) \frac{e^{ik_z|z-z_n|}}{k_z} e^{-i\mathbf{k}_\perp \cdot \mathbf{r}_n^\perp} \tilde{u}^*(\mathbf{k}_\perp), \tag{D3}$$

where $\tilde{u}(\mathbf{k}_\perp) = \frac{1}{2\pi}\int_{-\infty}^{\infty} e^{-i\mathbf{k}_\perp \cdot \mathbf{r}_\perp} u(\mathbf{r}_\perp) d\mathbf{r}_\perp$ is the Fourier transform of the transverse mode. We now consider the paraxial approximation in which the width of the spatial transverse mode $u(\mathbf{r}_\perp)$ is much larger than the wavelength, $w \gg \lambda$, and we consider propagation distances within its Rayleigh range $z < z_R = \pi w^2/\lambda$, so diffraction of the mode can be ignored. In Fourier space this means that $\tilde{u}(\mathbf{k}_\perp)$ has a very narrow width of approximately $2\pi/w$ around $\mathbf{k}_\perp = 0$, allowing us to approximate $k_z = \sqrt{k_p^2 - |\mathbf{k}_\perp|^2} \approx k_p$ and $\frac{|\mathbf{k}_\perp \cdot \mathbf{e}_d|^2}{k_p^2} \ll 1$; the requirement $z < z_R$ further allows us to approximate the phase factor $e^{ik_z|z-z_n|} \approx e^{ik_p|z-z_n|}$. Under these approximations, we obtain [by further transformation of $\tilde{u}^*(\mathbf{k}_\perp)$ back to real space]

$$\hat{E}_u(z) = \hat{E}_{u,0}(z) + \frac{idk_p}{2\epsilon_0\sqrt{A_u}} \sum_n u^*(\mathbf{r}_n^\perp) e^{ik_p|z-z_n|} \hat{\sigma}_{ge,n}. \tag{D4}$$

Decomposing $\hat{E}_u(z)$ into $\hat{E}_u^+(z)$ and $\hat{E}_u^-(z)$, which are the right-propagating and left-propagating fields [including only $k_z > 0$ or $k_z < 0$, respectively], sampled at $z > z_{\max}$ and $z < z_{\min}$, respectively ($z_n \in [z_{\min}, z_{\max}]$), we arrive at Eq. (17).

2. The input-field term Eq. (26)

For the mapping of the atomic equation (22) to the 1D model, we diagonalized the equation assuming that the condition (23) is valid. Here we give some details on the mapping of the input-field term. We introduce a complete basis $\{u_\beta(\mathbf{r}_\perp)\}$ that spans the function space of the x-y plane, such that $\sum_\beta u_\beta(\mathbf{r}_\perp) u_\beta^*(\mathbf{r}'_\perp) = \delta(\mathbf{r}_\perp - \mathbf{r}'_\perp)$. In the case of a Gaussian mode, the basis is the Hermite Gauss modes and $u(\mathbf{r}_\perp) \equiv u_0(\mathbf{r}_\perp)$ is the Gaussian mode $\beta = 0$. With this basis, the photon field can be written as an inverse transformation $\hat{E}(\mathbf{r}_\perp, z) = \sum_\beta \sqrt{A_\beta} \hat{E}_\beta(z) u_\beta(\mathbf{r}_\perp)$, and so

$$\frac{id}{\hbar} a_{\text{eff}} \sum_n \hat{E}_0(\mathbf{r}_n^\perp, 0) u^*(\mathbf{r}_n^\perp) = \\ = \frac{id}{\hbar} a_{\text{eff}} \sqrt{A_u} \hat{E}_{u,0}(0) \sum_n u^*(\mathbf{r}_n^\perp) u(\mathbf{r}_n^\perp) \\ + \frac{id}{\hbar} a_{\text{eff}} \sum_{\beta \neq 0} \sqrt{A_\beta} \hat{E}_{\beta,0}(0) \sum_n u_\beta(\mathbf{r}_n^\perp) u^*(\mathbf{r}_n^\perp) \\ = i\sqrt{\Gamma} \hat{\mathcal{E}}_0(0) + \hat{F}_0. \tag{D5}$$

Here we assumed that only the (Gaussian) $u(\mathbf{r}_\perp)$ mode, with $\beta = 0$, is populated, and the quantum noise operator $\hat{F}_0 = \frac{id}{\hbar} a_{\text{eff}} \sum_{\beta \neq 0} \sqrt{A_\beta} \hat{E}_{\beta,0}(0) \sum_n u_\beta^*(\mathbf{r}_n^\perp) u(\mathbf{r}_n^\perp)$ accounts for the vacuum fluctuations of other modes.

3. The upper bound on Γ

Here we prove that the total collective decay rate of the atomic system, $\Gamma_0 = 2\text{Re}[D_0]$, is always greater than or equal to the coupling to the target mode Γ, ensuring the self-consistency of our formalism. We recall that here D_0 is the eigenvalue of the dipole-dipole interaction kernel that corresponds to the relevant eigenmode, $v_{0,n} = a_{\text{eff}} u^*(\mathbf{r}_n^\perp)$,

$$D_0 = \sum_{n,m} v_{0,n} D_{nm} v_{0,m} \\ = -i\frac{3}{2}\lambda\gamma \sum_{n,m} v_{0,n} G(\omega_p, \mathbf{r}_n^\perp - \mathbf{r}_m^\perp, 0) v_{0,m}. \tag{D6}$$

Using again the in-plane momentum expansion of the Green's function, Eq. (D2), we obtain

$$D_0 = \frac{3}{4}\lambda\gamma \int_{-\infty}^{\infty} \frac{d\mathbf{k}_\perp}{4\pi^2} \left(1 - \frac{|\mathbf{k}_\perp \cdot \mathbf{e}_d|^2}{k_p^2}\right) \frac{|v_{0,\mathbf{k}_\perp}|^2}{\sqrt{k_p^2 - |\mathbf{k}_\perp|^2}}, \tag{D7}$$

with $v_{0,\mathbf{k}_\perp} = \sum_n v_{0,n} e^{-i\mathbf{k}_\perp \cdot \mathbf{r}_n^\perp}$ being the Fourier transform of the eigenmode, and where we assumed that $v_{0,n}$ is real (verified in all cases considered). From the square-root term, we note that the real part, which describes radiation, contains only in-plane momenta within the light cone, $|\mathbf{k}_\perp| < k_p$, as expected. In turn, the radiated field from the discrete-space paraxial eigenmode $v_{0,n}$ should be similar to its corresponding continuous-space interpolation given by the target mode $u(\mathbf{r}_\perp)$. Therefore, since in momentum space the target mode is narrow around $\mathbf{k}_\perp = 0$ (being paraxial), so is $v_{\mathbf{k}_\perp}$ within the light cone. For the real part,

this then allows us to approximate $1-\frac{|\mathbf{k}_\perp\cdot\mathbf{e}_d|^2}{k_p^2}\approx 1$ and $\sqrt{k_p^2-|\mathbf{k}_\perp|^2}\approx k_p$ within the integrand, obtaining

$$\Gamma_0 = 2\mathrm{Re}[D_0] = \frac{3}{4\pi}\lambda^2\gamma\int_{-\infty}^{\infty}\frac{d\mathbf{k}_\perp}{4\pi^2}|v_{0,\mathbf{k}_\perp}|^2. \tag{D8}$$

Moreover, since the target mode is normalized, we can multiply the right-hand-side of Eq. (D8) by $1=\int_{-\infty}^{\infty}\frac{d\mathbf{k}_\perp}{4\pi^2}|\tilde{u}(\mathbf{k}_\perp)|^2$, and using the Cauchy–Schwarz inequality, we obtain

$$\begin{aligned}\Gamma_0 &= \frac{3}{4\pi}\lambda^2\gamma\int_{-\infty}^{\infty}\frac{d\mathbf{k}_\perp}{4\pi^2}\left|v_{0,\mathbf{k}_\perp}\right|^2\int_{-\infty}^{\infty}\frac{d\mathbf{k}'_\perp}{4\pi^2}\left|\tilde{u}(\mathbf{k}'_\perp)\right|^2\\ &\geq \frac{3}{4\pi}\lambda^2\gamma\left|\int_{-\infty}^{\infty}\frac{d\mathbf{k}_\perp}{4\pi^2}v_{0,\mathbf{k}_\perp}\tilde{u}^*(\mathbf{k}_\perp)\right|^2.\end{aligned} \tag{D9}$$

In turn, we note, also using Eq. (20) for a_{eff}, that

$$\begin{aligned}&\left|\int_{-\infty}^{\infty}\frac{d\mathbf{k}_\perp}{4\pi^2}v_{0,\mathbf{k}_\perp}\tilde{u}^*(\mathbf{k}_\perp)\right|^2\\ &=\left|\int_{-\infty}^{\infty}\frac{d\mathbf{k}_\perp}{4\pi^2}\sum_n v_{0,n}e^{-i\mathbf{k}_\perp\cdot\mathbf{r}_n^\perp}\tilde{u}^*(\mathbf{k}_\perp)\right|^2\\ &=\left|\sum_n a_{\mathrm{eff}}u^*(\mathbf{r}_n^\perp)\int_{-\infty}^{\infty}\frac{d\mathbf{k}_\perp}{4\pi^2}e^{-i\mathbf{k}_\perp\cdot\mathbf{r}_n^\perp}\tilde{u}^*(\mathbf{k}_\perp)\right|^2\\ &=a_{\mathrm{eff}}^2\left|\sum_n|u^*(\mathbf{r}_n^\perp)|^2\right|^2=\frac{1}{a_{\mathrm{eff}}^2}.\end{aligned} \tag{D10}$$

Finally, inserting this into Eq. (D9) and using Eq. (28) for Γ, we obtain the required inequality,

$$\Gamma_0\geq\frac{3}{4\pi}\frac{\lambda^2}{a_{\mathrm{eff}}^2}\gamma=\Gamma. \tag{D11}$$

APPENDIX E: MAPPING THE 2D ORDERED ARRAY TO THE 1D MODEL

In the following, we show that the collective dipole mode $\hat{P}$ that corresponds to an arbitrary paraxial target mode $u(\mathbf{r}_\perp)$ forms an approximate eigenmode of the dipole-dipole interaction kernel of a finite-size 2D ordered array, with an eigenvlaue $D_0=\Gamma_{\mathbf{k}=0}/2+i\Delta_{\mathbf{k}=0}$ equal to that of a plane wave eigenmode $\mathbf{k}_\perp=0$ of an infinite 2D array.

To show this we focus on the dipole-dipole interaction term in the second line of Eq. (14), projected to the paraxial target mode via the transformation (19) with $a_{\mathrm{eff}}=\frac{a}{\sqrt{\eta}}$,

$$\frac{a}{\sqrt{\eta}}i\frac{3}{2}\gamma\lambda\sum_n\sum_m G(\omega_p,\mathbf{r}_n^\perp-\mathbf{r}_m^\perp,0)\hat{\sigma}_{ge,m}u^*(\mathbf{r}_n^\perp), \tag{E1}$$

where $\frac{d^2\omega_p^2}{\hbar\epsilon_0c^2}=(3/2)\gamma\lambda$ was used. Considering the inverse Fourier transformation of the target mode, $u(\mathbf{r}_\perp)=(1/2\pi)\int\tilde{u}(\mathbf{k}_\perp)e^{i\mathbf{k}_\perp\cdot\mathbf{r}_\perp}d\mathbf{k}_\perp$, we obtain

$$\begin{aligned}&=\frac{a}{\sqrt{\eta}}i\frac{3}{2}\gamma\lambda\sum_m\hat{\sigma}_{ge,m}\frac{1}{2\pi}\\ &\quad\times\int d\mathbf{k}_\perp\tilde{u}^*(\mathbf{k}_\perp)G_m(\omega_p,\mathbf{k}_\perp,0)e^{-i\mathbf{k}_\perp\cdot\mathbf{r}_m^\perp},\end{aligned} \tag{E2}$$

where we defined $G_m(\omega_p,\mathbf{k}_\perp,0)=\sum_n G(\omega_p,\mathbf{r}_n^\perp-\mathbf{r}_m^\perp,0)e^{-i\mathbf{k}_\perp\cdot(\mathbf{r}_n^\perp-\mathbf{r}_m^\perp)}$. Next we assume that the array is larger than the wavelength $L_a\gg\lambda\rightarrow\sqrt{N}\gg\lambda/a$, so each atom in the "bulk" (not at the edges) effectively feels interactions of an infinite array (our noting the Green's function oscillation length scale λ). This assumption also implies that $\sqrt{N}\gg 1$, so most of the atoms are in the bulk, and are therefore dominant in the description of collective dipole modes. Under these conditions, we can consider $G_m(\omega_p,\mathbf{k}_\perp,0)$ as that of an atom m in the bulk, for which $G_m(\omega_p,\mathbf{k}_\perp,0)\approx G(\omega_p,\mathbf{k}_\perp,0)=\sum_{n\in\mathrm{infinite}}G(\omega_p,\mathbf{r}_n^\perp,0)e^{-i\mathbf{k}_\perp\cdot\mathbf{r}_n^\perp}$, where $G(\omega_p,\mathbf{k}_\perp,0)$ is for an infinite array. Then, considering the paraxial character of the target mode, we assume that $\tilde{u}^*(\mathbf{k}_\perp)$ is centered at $\mathbf{k}_\perp=0$ at a bandwidth much narrower than that of the Green's function $G(\omega_p,\mathbf{k}_\perp,0)$ [29], such that the latter is effectively sampled at $\mathbf{k}_\perp=0$, giving

$$\begin{aligned}&=\frac{a}{\sqrt{\eta}}i\frac{3}{2}\gamma\lambda G(\omega_p,0,0)\sum_m\hat{\sigma}_{ge,m}u^*(\mathbf{r}_m^\perp)\\ &=-\left(\frac{\Gamma_{\mathbf{k}=0}}{2}+i\Delta_{\mathbf{k}=0}\right)\hat{P},\end{aligned} \tag{E3}$$

where we used the transformation (19) to $\hat{P}$ with $a_{\mathrm{eff}}=\frac{a}{\sqrt{\eta}}$. This result shows that the dipole-dipole kernels exhibits a diagonal form for the collective dipole mode $\hat{P}$, with a corresponding eigenvalue $i\frac{3}{2}\gamma\lambda G(\omega_p,0,0)=\frac{\Gamma_{\mathbf{k}=0}}{2}+i\Delta_{\mathbf{k}=0}$. The latter is simply the collective decay and shift of the uniform collective dipole of an infinite array [29], thus giving the result expressed in Eq. (33).

APPENDIX F: MAPPING THE MULTILAYER SYSTEM TO THE 1D MODEL

Here we elaborate on the extension of the mapping procedure to a multilayer system discussed in Sec. VII. First,

we perform the transformation (37) on Eq. (14) for $\hat{\sigma}_{ge,n_\perp j}$ [with the replacement $(\mathbf{r}_n^\perp, z_n) \to (\mathbf{r}_{n_\perp}^\perp, z_j)$], obtaining

$$\frac{d\hat{P}_j}{dt} = \left(i\delta_p - \frac{\gamma_s}{2}\right)\hat{P}_j + i\Omega\hat{S}_j + i\frac{d}{\hbar}\hat{E}_{0,j} + \hat{F}_{u,j} - a_{\text{eff}}\sum_{n_\perp} u^*(\mathbf{r}_{n_\perp}^\perp)\sum_{m_\perp}\sum_{j'} D_{n_\perp,m_\perp}(z_j - z_{j'})\hat{\sigma}_{ge,m_\perp j'}, \tag{F1}$$

with $D_{n_\perp,m_\perp}(z_j - z_{j'}) = \frac{i}{\hbar}\frac{d^2\omega_p^2}{\epsilon_0 c^2}G(\omega_p, \mathbf{r}_{n_\perp}^\perp - \mathbf{r}_{m_\perp}^\perp, z_j - z_{j'})$ and $\hat{E}_{0,j} = a_{\text{eff}}\sum_n u^*(\mathbf{r}_n^\perp)\hat{E}_0(\mathbf{r}_\perp, z_j)$ (and an analogous definition for $\hat{F}_{u,j}$). We split the summation over the layers into the self-interacting term $j = j'$, which can be treated as in the single-layer case (see Appendix D),

$$a_{\text{eff}}\sum_{n_\perp} u^*(\mathbf{r}_{n_\perp}^\perp)\sum_{m_\perp} D_{n_\perp,m_\perp}(0)\hat{\sigma}_{ge,m_\perp j} = \left(\frac{\Gamma_0}{2} + i\Delta\right)\hat{P}_j, \tag{F2}$$

and the interlayer interaction term $j \neq j'$,

$$a_{\text{eff}}\sum_{n_\perp} u^*(\mathbf{r}_{n_\perp}^\perp)\sum_{m_\perp}\sum_{j'\neq j} D_{n_\perp,m_\perp}(z_j - z_{j'})\hat{\sigma}_{ge,m_\perp j'}. \tag{F3}$$

Using the in-plane momentum expansion of the Green's function, Eq. (D2), we obtain

$$= a_{\text{eff}}\frac{3}{4}\lambda\gamma\sum_{n_\perp} u^*(\mathbf{r}_{n_\perp}^\perp)\sum_{m_\perp}\sum_{j'\neq j}\int_{-\infty}^{\infty}\frac{d\mathbf{k}_\perp}{4\pi^2}\left(1 - \frac{|\mathbf{k}_\perp\cdot\mathbf{e}_d|^2}{k_p^2}\right) \times e^{i\mathbf{k}_\perp\cdot\left(\mathbf{r}_{n_\perp}^\perp - \mathbf{r}_{m_\perp}^\perp\right)}\frac{e^{ik_z|z_j - z_{j'}|}}{k_z}\hat{\sigma}_{ge,m_\perp j'}. \tag{F4}$$

We assume that the target mode is equal to the eigenmode $l = 0$, $a_{\text{eff}}u^*(\mathbf{r}_{n_\perp}^\perp) = v_{0,n}$, and using $v_{0,\mathbf{k}_\perp} = \sum_n v_{0,n}e^{-i\mathbf{k}_\perp\cdot\mathbf{r}_n^\perp}$, we can write

$$= \frac{3}{4}\lambda\gamma\sum_{m_\perp}\sum_{j'\neq j}\int_{-\infty}^{\infty}\frac{d\mathbf{k}_\perp}{4\pi^2}\left(1 - \frac{|\mathbf{k}_\perp\cdot\mathbf{e}_d|^2}{k_p^2}\right)v_{0,-\mathbf{k}_\perp}e^{-i\mathbf{k}_\perp\cdot\mathbf{r}_{m_\perp}^\perp} \times \frac{e^{ik_z|z_j - z_{j'}|}}{k_z}\hat{\sigma}_{ge,m_\perp j'}. \tag{F5}$$

The term $e^{ik_z|z_j - z_{j'}|}$ includes interactions between different layers via propagating fields and evanescent fields, corresponding to in-plane momentum components inside and outside the light cone, i.e., $|\mathbf{k}_\perp| < k_p$ (real k_z) and $|\mathbf{k}_\perp| > k_p$ (imaginary k_z), respectively. However, assuming that $|z_j - z_{j'}| > 1/k_p \sim \lambda$ for all z_j and $z_{j'}$, the exponentially decaying contribution of the evanescent fields is negligible (we discuss a correction due to these near fields in the case of an ordered array in Appendix H). In turn, inside the light cone $|\mathbf{k}_\perp| \leq k_p$, the eigenmode $v_{0,\mathbf{k}_\perp}$ is narrow since the target mode is paraxial (see also Appendix D 3). Taking in addition $|z_j - z_{j'}| < \pi w^2/\lambda = z_R$ for all z_j and $z_{j'}$, we can thus approximate $e^{ik_z|z_j - z_{j'}|} \approx e^{ik_p|z_j - z_{j'}|}$, obtaining

$$= \sum_{j'\neq j} e^{ik_p|z_j - z_{j'}|}a_{\text{eff}}\frac{3}{4}\lambda\gamma\sum_{n_\perp} u^*(\mathbf{r}_{n_\perp}^\perp)\sum_{m_\perp} \int_{\text{LC}}\frac{d\mathbf{k}_\perp}{4\pi^2}\left(1 - \frac{|\mathbf{k}_\perp\cdot\mathbf{e}_d|^2}{k_p^2}\right)e^{i\mathbf{k}_\perp\cdot\left(\mathbf{r}_{n_\perp}^\perp - \mathbf{r}_{m_\perp}^\perp\right)}\frac{1}{k_z}\hat{\sigma}_{ge,m_\perp j'}. \tag{F6}$$

Noting that the above expression is equal to $\sum_{j'\neq j} e^{ik_p|z_j - z_{j'}|}$ multiplied by the real part of the analogous term in the single-layer case, Eq. (F2), we have

$$= \frac{\Gamma_0}{2}\sum_{j'\neq j} e^{ik_p|z_j - z_{j'}|}\hat{P}_j. \tag{F7}$$

The field term $i(d/\hbar)\hat{E}_{0,j}$ is treated as in Eq. (D5), giving $i(d/\hbar)\hat{E}_{0,j} = i\sqrt{\Gamma_{1\text{D}}}\hat{\mathcal{E}}_{0,j} + \hat{F}_{0,j}$, with $\hat{\mathcal{E}}_{0,j} = [\hat{\mathcal{E}}_{0,+}(z_j) + \hat{\mathcal{E}}_{0,-}(z_j)]/\sqrt{2}$. Collecting everything together we have

$$\frac{d\hat{P}_j}{dt} = \left[i(\delta_p - \Delta) - \frac{\gamma_s}{2}\right]\hat{P}_j - \frac{\Gamma_0}{2}\sum_{j'=1}^{N_z} e^{ik_p|z_j - z_{j'}|}\hat{P}_{j'} + i\sqrt{\Gamma_{1\text{D}}}\hat{\mathcal{E}}_{0,j} + i\Omega\hat{S}_j + \hat{F}_j, \tag{F8}$$

with $\hat{F}_j = \hat{F}_{u,j} + \hat{F}_{0,j}$, yielding Eq. (38).

For the input-field term, we use Eqs. (27) and (16) with $\hat{a}_{uk_z}(t) \to \hat{a}_{uk_z}(0)e^{-ic|k_z|t}$ (for the free, input field) to obtain

$$\hat{\mathcal{E}}_{0,j} = \frac{1}{\sqrt{2}}[\hat{\mathcal{E}}_{0,+}(z_j) + \hat{\mathcal{E}}_{0,-}(z_j)] = i\sqrt{\frac{c}{2L}}\sum_{k_z\geq 0}\left[\hat{a}_{u,+k_z}e^{ik_z z_j} + \hat{a}_{u,-k_z}e^{-ik_z z_j}\right]e^{-i(c|k_z| - \omega_p)t}. \tag{F9}$$

We now wish to approximate the phase factors $e^{\pm ik_z z_j} \approx e^{\pm ik_p z_j}$, which is justified if the correction $\Delta k z_j < \Delta k L_{\max} \ll 1$ is small, where here Δk is the bandwidth of k_z around k_p accounted for by our theory and $L_{\max}$ is the maximal interatomic distance. Recalling that within the paraxial approximation we have $\omega_{k_z} \approx c|k_z|$, we find that the bandwidth on k_z follows the bandwidth of frequencies, $\Delta\omega \gtrsim \tau_s^{-1}$, which is determined by the temporal resolution required to describe system dynamics $\tau_s \sim \gamma^{-1}$. This condition for a small phase correction $\Delta k L_{\max} \ll 1$ then translates to the condition $\tau_s \gg L_{\max}/c$. This condition is consistent with the Markov approximation used

to derive the Heisenberg-Langevin equation (14), wherein the maximal propagation time of photons that mediate the dipole-dipole interaction, $L_{\max}/c$, is assumed to be shorter than the dynamics of the system τ_s. With this reasonable assumption, and considering the Bragg condition $e^{ik_p z_j} = e^{-ik_p z_j}$, we have

$$\hat{\mathcal{E}}_{0,j} = i\sqrt{\frac{c}{2L}} \sum_{k_z \geq 0} \left[\hat{a}_{u+k_z} + \hat{a}_{u-k_p}\right] e^{-i(c|k_z|-\omega_p)t} e^{ik_p z_j}$$
$$= e^{ik_p z_j} \frac{1}{\sqrt{2}} [\hat{\mathcal{E}}_{0,+}(0) + \hat{\mathcal{E}}_{0,-}(0)] = e^{ik_p z_j} \hat{\mathcal{E}}_0(0). \quad \text{(F10)}$$

Finally, performing the transformation to the phase-matched collective dipole $\hat{P}$, Eq. (39), on Eq. (F8) and recalling the Bragg condition $e^{-ik_p z_j} = e^{ik_p z_j}$, we obtain the 1D model equation (6) for $\hat{P}$ with the parameters specified in Eq. (40).

For the field equation we start with the analogue of Eq. (D4), with an additional summation over the layers, obtaining

$$\hat{E}_u(z) = \hat{E}_{u,0}(z) + \frac{idk_p}{2\epsilon_0\sqrt{A_u}} \frac{1}{a_{\text{eff}}} \sum_{j=1}^{N_z} e^{ik_p|z-z_j|} \hat{P}_j. \quad \text{(F11)}$$

The difference from the single-layer case is that now each layer has an extra relative phase proportional to its position along the z axis. Under the Bragg condition, this phase is identical for all layers up to a sign, yielding the same sign for $2z_j/\lambda$ even or alternating signs for $2z_j/\lambda$ odd. In either case, the phase of each layer matches the phase of the collective dipole $\hat{P}_j$. With these considerations, the input-output relation for the symmetric field $\hat{\mathcal{E}}(z) = \frac{1}{\sqrt{2}}\left[\hat{\mathcal{E}}_+(z) + \hat{\mathcal{E}}_-(-z)\right] e^{-ik_p z}$ $(z > 0)$ reduces to

$$\hat{\mathcal{E}}(z) = \hat{\mathcal{E}}_0(z) + i\sqrt{N_z \Gamma_{1D}} \hat{P}, \quad \text{(F12)}$$

again consistent with the 1D model (6) with the parameters from Eq. (40).

APPENDIX G: MULTILAYER SYSTEM BEYOND THE BRAGG CONDITION

In this appendix, we investigate the propagation of light within the multilayer system with arbitrary interlayer spacing, and in particular when the Bragg condition is not satisfied and the connection to the OD can be established. Our starting point is Eq. (38) for the coupling between layers, in the form of 1D propagation. We consider the case $\Gamma_0 = \Gamma_{1D}$, wherein the interlayer 1D propagation is channeled via only the target mode. This means that collective effects between layers are mediated via only the target mode and do not contribute to the losses, which are due to only the individual loss of each layer, γ_s (as in the case of perfect spatial overlap $\eta = 1$ for the example of a 3D ordered array). Such lossy 1D propagation is naturally accounted for by the transfer matrix method [71,72]. This method enables the calculation of the transmission and reflection coefficients of a series of optical elements by assigning a matrix to each element that connects forward-propagating and backward-propagating waves from each side, thereby accounting for all interference effects. In our multilayer system, all elements are identical and comprise a single layer followed by free propagation over a distance a_z (see Fig. 9). The transfer matrix of each such element is

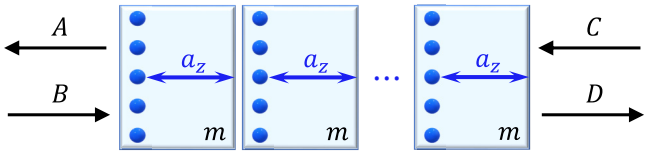

FIG. 9. Multilayer system represented as a series of building blocks (optical elements), each comprising a single layer followed by a propagation over distance a_z. The input and output are divided into forward and backward propagation on the left-hand and right-hand sides of the multilayer system.

$$m = \frac{1}{t_1} \begin{pmatrix} t_1^2 - r_1^2 & r_1 \\ -r_1 & 1 \end{pmatrix} \begin{pmatrix} e^{ik_p a_z} & 0 \\ 0 & e^{-ik_p a_z} \end{pmatrix}, \quad \text{(G1)}$$

where $r_1 = -\frac{\Gamma_{1D}}{\Gamma_{1D}+\gamma_s+2i(\Delta-\delta_p)}$ and $t_1 = 1 + r_1$ are the reflectivity and transmissivity of a single layer. The transfer matrix for a system comprising N_z layers is then $M = m^{N_z}$, connecting the right and left fields as $(A, B)^T = M \cdot (C, D)^T$ (Fig. 9). The reflection and transmission coefficients associated with the multilayer system are given by $r = M_{12}/M_{22}$ and $t = 1/M_{22}$, allowing us to easily compute them numerically.

In principle, the overall propagation is composed of multiple scattering of backward-propagating and forward-propagating waves. In the following, we discuss two important regimes, where backscattering is dominant and absent, respectively. For the former, we consider the lattice spacing $a_z/\lambda = 0.5$ satisfying the Bragg condition, as assumed in our theory of the mapping to the two-sided 1D model. In Fig. 10(a), we observe the agreement between the transfer matrix calculation and the theoretical prediction of Eq. (40), $r = -\frac{N_z\Gamma_{1D}}{\Gamma_{N_z 1D}+\gamma_s+2i(\Delta-\delta_p)}$. Notably, even in the presence of significant loss terms, $\gamma_s \gg \Gamma_{1D}$, the addition of layers in phase-matching Bragg conditions results in a remarkably high reflectivity. In contrast, consider now the case $a_z/\lambda = 0.25$, which deviates significantly from the Bragg condition. Since in this case phase matching in reflection does not exist, we expect backscattering to be negligible, and forward-only propagation (as with Bloch waves in the middle of the band). Indeed, we observe in Fig. 10(b) that the reflectance is substantially diminished. In turn, the transmittance exhibits an exponential decay

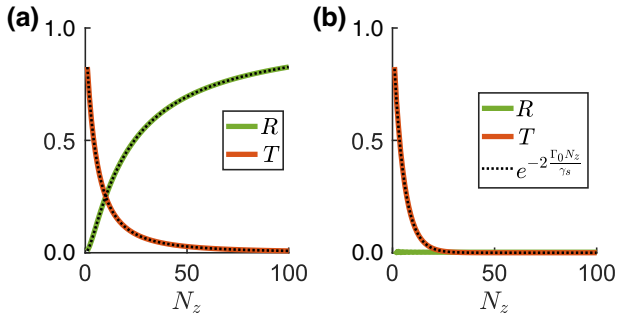

FIG. 10. Intensity transmittance (T) and reflectance (R) as a function of the number of layers N_z for interlayer spacing (a) $a_z/\lambda = 0.5$ and (b) $a_z/\lambda = 0.25$. Solid and dotted lines represent transfer-matrix numerical calculations and theoretical analytical predictions, respectively (see the text). In both plots the ratio between individual losses and collective emission to the target mode of each layer is taken to be $\gamma_s/\Gamma_{1D} = 10$.

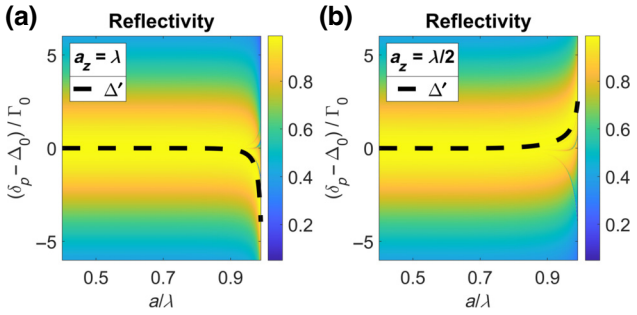

FIG. 11. Intensity reflection coefficient R of a 3D multilayered array as a function of detuning $\delta_p - \Delta$ and the ratio a/λ for (a) $a_z = \lambda$, and (b) $a_z = \lambda/2$. The detuning correction Δ' (dashed line) fits the maximal reflectivity. The reflectivity was calculated for an array with $N_z = 10$, $\eta = 1$, and $\gamma_{\text{loss}} = 0.05\Gamma_0$.

with the number of layers N_z due to the losses γ_s. Such lossy, forward-only propagation can be connected to the concept of OD in dilute atomic ensembles. Estimating the transmittance analytically in the regime of a large loss rate ($\gamma_s \gg \Gamma_0$) on resonance, we find that the intensity transmittance follows an exponential decrease with N_z, $\exp\left(-2\frac{\Gamma_0 N_z}{\gamma_s}\right) = e^{-2\text{OD}}$, exhibiting excellent agreement with the transfer matrix calculation [Fig. 10(b)]. We thus find that the OD is equal to the cooperativity $C = \Gamma_{1D}N_z/\gamma_s$ of the analogous two-sided phase-matched system considered in our work [Eq. (40)].

Importantly, while both regimes are characterized by the same light-matter coupling strength ($C = \text{OD}$), their response to light is very different: the extinction in transmittance in the two-sided phase-matched system is due to its strong reflection and it exhibits a power-law decrease with N_z, $t = 1 + r \propto N_z^{-1}$, whereas in the non-phase-matched system, characterized by an OD, the extinction in transmittance is due to losses and it decays exponentially with N_z.

APPENDIX H: CORRECTION Δ′ TO THE 3D ARRAY COLLECTIVE SHIFT

Here we elaborate on the estimation of the correction Δ' to the collective shift, as discussed in Sec. VII subsection C2 for the collective dipole $\hat{P}$ of a 3D ordered array. First, to get Eq. (38) for 2D array layers $\hat{P}_j$ with the full dipole-dipole kernel $\mathcal{D}_{jj'}$ from Eq. (42) replacing the 1D-like dipole-dipole kernel $(\Gamma_0/2)e^{ik_p|z_j - z_{j'}|}$, we do the following: Starting from Eq. (14) and performing the transformation to $\hat{P}_j$, we obtain the interaction term in analogy to that in Eq. (E1) in the 2D array case, with the Green's function now having a z-axis argument, $G(\omega_p, \mathbf{r}^{\perp}_{n_\perp} - \mathbf{r}^{\perp}_{m_\perp}, a_z(j - j'))$. Using methods similar to those described in Appendix E, we then arrive at the interlayer dipole-dipole kernel

$$\mathcal{D}_{jj'} = -\frac{i}{\hbar}\frac{d^2\omega_p^2}{\epsilon_0 c^2} G(\omega_p, \mathbf{k}_\perp = 0, a_z(j - j')), \tag{H1}$$

where $G(\omega_p, \mathbf{k}_\perp, z) = \sum_{n_\perp \in \text{infinite}} G(\omega_p, \mathbf{r}^{\perp}_{n_\perp}, z)e^{-i\mathbf{k}_\perp \cdot \mathbf{r}^{\perp}_{n_\perp}}$ is evaluated for a sum over an infinite array. The latter sum is performed with the transverse-momentum presentation of the Green's function as in Ref. [29], yielding Eq. (42) for $\mathcal{D}_{jj'}$.

As explained in the main text, the correction Δ' to the collective shift comes from a perturbative treatment of the evanescent-field component, $\varepsilon_{j,j'}$, of the interaction $\mathcal{D}_{jj'}$ between layers; see Eq. (44). To first order in perturbation theory, the correction to the relevant collective eigenmode from Eq. (39), $|v\rangle = (1/\sqrt{N_z})\left(1, e^{-ik_p a_z j}, \ldots, e^{-ik_p a_z N_z}\right)$, is given as usual by the matrix element $\langle v|\varepsilon|v\rangle$,

$$\Delta' = \frac{1}{N_z}\sum_{j \neq j'} e^{ik_p(z_{n_z} - z_{m_z})}\varepsilon_{j,j'}. \tag{H2}$$

We now verify that this approximation is sufficiently accurate for relevant cases. To this end, we consider the calculation of the 3D array reflectivity in two ways. From the mapping to the generic 1D model (1), we readily predict that the optimal reflectivity is obtained at a resonance *shifted* by Δ', i.e., for $\delta_p = \Delta + \Delta'$, using Δ' from Eq. (H2). This is compared with an exact calculation that does not rely on the first-order perturbative approximation of Eq. (H2) and the subsequent mapping to the generic 1D model. Beginning with Eq. (38) with the full interlayer kernel from (42) (including $\varepsilon_{j,j'}$), we classically solve for the dipole P_j of the layer j given a cw input field using a simple matrix inversion performed numerically. Then, plugging this solution into Eq. (F11), we find the total field and the reflectivity. The results of this exact numerical calculation for the example of an ordered array are presented in Fig. 11 as a function of the detuning and the ratio a/λ and for both types of phase-matched collective dipoles,

i.e., $a_z = \lambda$ and $a_z = \lambda/2$. Maximal reflectivity is indeed observed to overlap the curve of $\Delta'(a/\lambda)$ calculated from Eq. (H2) as a function of a/λ, as predicted by the approximate generic 1D model with the shift Δ'. As a relevant example, consider the lattice spacing $a/\lambda = 0.68$ corresponding to a typical optical lattice experiment [30]: in this case, we see in Fig. 11 excellent agreement between the position of the maxima of the exact result and the corresponding value of Δ'. To conclude, we find that the mapping to the generic 1D model is valid for the regions of interest, using the small correction Δ'.

[1] A. I. Lvovsky, B. C. Sanders, and T. Wolfgang, Optical quantum memory, Nat. Photonics **3.12**, 706 (2009).

[2] D. E. Chang, V. Vuletić, and M. D. Lukin, Quantum nonlinear optics – photon by photon, Nat. Photonics **8**, 685 (2014).

[3] C. Liu, Z. Dutton, C. H. Behroozi, and L. V. Hau, Observation of coherent optical information storage in an atomic medium using halted light pulses, Nature **409**, 490 (2001).

[4] D. F. Phillips, A. Fleischhauer, A. Mair, R. L. Walsworth, and M. L. Lukin, Storage of light in atomic vapor, Phys. Rev. Lett. **86**, 783 (2001).

[5] B. Julsgaard, J. Sherson, J. Cirac, J. Fiurášek, and E. S. Polzik, Experimental demonstration of quantum memory for light, Nature **432**, 482 (2004).

[6] M. D. Eisaman, A. André, F. Massou, M. Fleischhauer, A. S. Zibrov, and M. D. Lukin, Electromagnetically induced transparency with tunable single-photon pulses, Nature (London) **438**, 837 (2005).

[7] T. Chanelière, D. Matsukevich, S. D. Jenkins, S.-Y. Lan, T. A. B. Kennedy, and A. Kuzmich, Storage and retrieval of single photons transmitted between remote quantum memories, Nature (London) **438**, 833 (2005).

[8] M. Fleischhauer, A. Imamoglu, and J. P. Marangos, Electromagnetically induced transparency: Optics in coherent media, Rev. Mod. Phys. **77**, 633 (2005).

[9] A. V. Gorshkov, A. André, M. Fleischhauer, A. S. Sørensen, and M. D. Lukin, Universal approach to optimal photon storage in atomic media, Phys. Rev. Lett. **98**, 123601 (2007).

[10] A. V. Gorshkov, A. André, N. D. Lukin, and A. S. Sørensen, Phys. Rev. A **76**, 033805 (2007).

[11] K. S. Cohi, H. Deng, J. Laurat, and H. J. Kimble, Mapping photonic entanglement into and out of a quantum memory, Nature **452**, 67 (2008).

[12] K. Hammerer, A. S. Sørensen, and E. S. Polzik, Quantum interface between light and atomic ensembles, Rev. Mod. Phys. **82**, 1041 (2010).

[13] O. Katz, R. Shaham, E. Reches, A. V. Gorshkov, and O. Firstenberg, Optical quantum memory for noble-gas spins based on spin-exchange collisions, Phys. Rev. A **105**, 042606 (2022).

[14] B. Gouraud, D. Maxein, A. Nicolas, O. Morin, and J. Laurat, Demonstration of a memory for tightly guided light in an optical nanofiber, Phys. Rev. Lett. **114**, 180503 (2015).

[15] C. Sayrin, C. Clausen, B. Albrecht, P. Schneeweiss, and A. Rauschenbeutel, Storage of fiber-guided light in a nanofiber-trapped ensemble of cold atoms, Optica **2**, 353 (2015).

[16] A. V. Gorshkov, A. André, N. D. Lukin, and A. S. Sørensen, Phys. Rev. A **76**, 033804 (2007).

[17] J. Ma, X. Wang, C. Sun, and F. Nori, Quantum spin squeezing, Phys. Rep. **509**, 89 (2011).

[18] L. I. R. Gil, R. Mukherjee, E. M. Bridge, M. P. A. Jones, and T. Pohl, Spin squeezing in a Rydberg lattice clock, Phys. Rev. Lett. **112**, 103601 (2014).

[19] N. Henkel, R. Nath, and T. Pohl, Three-dimensional roton excitations and supersolid formation in Rydberg-excited Bose-Einstein condensates, Phys. Rev. Lett. **104**, 195302 (2010).

[20] J. I. Cirac, P. Zoller, H. J. Kimble, and H. Mabuchi, Quantum state transfer and entanglement distribution among distant nodes in a quantum network, Phys. Rev. Lett. **78**, 3221 (1997).

[21] H. P. Specht, C. Nölleke, A. Reiserer, M. Uphoff, E. Figueroa, S. Ritter, and G. Rempe, A single-atom quantum memory, Nature **473**, 190 (2011).

[22] S. Ritter, C. Nölleke, C. Hahn, A. Reiseter, A. Neuzner, M. Uphoff, and G. Rempe, An elementary quantum network of single atoms in optical cavities, Nature **484**, 195 (2012).

[23] L. Giannelli, T. Schmit, T. Calarco, C. P. Koch, S. Ritter, and G. Morigi, Optimal storage of a single photon by a single intra-cavity atom, New J. Phys. **20**, 105009 (2018).

[24] M. Körber, O. Morin, S. Langenfeld, A. Neuzner, S. Ritter, and G. Rempe, Decoherence-protected memory for a single-photon qubit, Nat. Photonics **12**, 18 (2018).

[25] I. Bloch, Ultracold quantum gases in optical lattices, Nat. Phys. **1**, 23 (2005).

[26] I. Bloch, J. Dalibard, and S. Nascimbène, Quantum simulations with ultracold quantum gases, Nat. Phys. **8**, 267 (2012).

[27] G. Facchinetti, S. D. Jenkins, and J. Ruostekoski, Storing light with subradiant correlations in arrays of atoms, Phys. Rev. Lett. **117**, 1243601 (2016).

[28] R. J. Bettles, S. A. Gardiner, and C. S. Adams, Enhanced optical cross section via collective coupling of atomic dipoles in a 2D array, Phys. Rev. Lett. **116**, 103602 (2016).

[29] E. Shahmoon, D. S. Wild, M. D. Lukin, and S. F. Yelin, Cooperative resonances in light scattering from two-dimensional atomic arrays, Phys. Rev. Lett. **118**, 113601 (2017).

[30] J. Rui, D. Wei, A. Rubio-Abadal, S. Hollerith, J. Zeiher, D. M. Stamper-Kurn, C. Gross, and I. Bloch, A subradiant optical mirror formed by a single structured atomic layer, Nature **583**, 369 (2020).

[31] M. T. Manzoni, M. Moreno-Cardoner, A. Asenjo-Garcia, J. V. Porto, A. V. Gorshkov, and D. E. Chang, Optimization of photon storage fidelity in ordered atomic arrays, New J. Phys. **20**, 083048 (2018).

[32] A. Grankin, P.-O. Guimond, D. V. Vasilyev, B. Vermersch, and P. Zoller, Free-space photonic quantum link and chiral quantum optics, Phys. Rev. A **98**, 043825 (2018).

[33] P.-O. Guimond, A. Grankin, D. V. Vasilyev, B. Vermersch, and P. Zoller, Subradiant Bell states in distant atomic arrays, Phys. Rev. Lett. **122**, 093601 (2019).

[34] L. Henriet, J. S. Douglas, D. E. Chang, and A. Albrecht, Critical open-system dynamics in a one-dimensional optical-lattice clock, Phys. Rev. A **99**, 023802 (2019).
[35] E. Shahmoon, M. D. Lukin, and S. F. Yelin, *Advances in Atomic, Molecular, and Optical Physics* (Elsevier, Amsterdam, 2019), Vol. 68, p. 1.
[36] E. Shahmoon, M. D. Lukin, and S. F. Yelin, Quantum optomechanics of a two-dimensional atomic array, Phys. Rev. A **101**, 063833 (2020).
[37] E. Shahmoon, D. S. Wild, M. D. Lukin, and S. F. Yelin, Cavity quantum optomechanics with an atom-array membrane, arXiv:2006.01973.
[38] C. D. Parmee and J. Ruostekoski, Bistable optical transmission through arrays of atoms in free space, Phys. Rev. A **103**, 033706 (2021).
[39] A. Asenjo-Garcia, M. Moreno-Cardoner, A. Albrecht, H. J. Kimble, and D. E. Chang, Exponential improvement in photon storage fidelities using subradiance and "selective radiance" in atomic arrays, Phys. Rev. X **7**, 031024 (2017).
[40] S. J. Masson and A. Asenjo-Garcia, Atomic-waveguide quantum electrodynamics, Phys. Rev. Res. **2**, 043213 (2020).
[41] T. L. Patti, D. S. Wild, E. Shahmoon, M. D. Lukin, and S. F. Yelin, Controlling interactions between quantum emitters using atom arrays, Phys. Rev. Lett. **126**, 223602 (2021).
[42] D. Castells-Graells, D. Malz, C. C. Rusconi, and J. I. Cirac, Atomic waveguide QED with atomic dimers, Phys. Rev. A **104**, 063707 (2021).
[43] J. Perczel, J. Borregaard, D. E. Chang, H. Pichler, S. F. Yelin, P. Zoller, and M. D. Lukin, Topological quantum optics in two-dimensional atomic arrays, Phys. Rev. Lett. **119**, 023603 (2017).
[44] R. J. Bettles, J. Minar, C. S. Adams, I. Lesanovsky, and B. Olmos, Topological properties of a dense atomic lattice gas, Phys. Rev. A **96**, 041603(R) (2017).
[45] D. Plankensteiner, C. Sommer, H. Ritsch, and C. Genes, Cavity antiresonance spectroscopy of dipole coupled subradiant arrays, Phys. Rev. Lett. **119**, 093601 (2017).
[46] E. Shahmoon, D. S. Wild, M. D. Lukin, and S. F. Yelin, Theory of cavity QED with 2D atomic arrays, arXiv:2006.01972.
[47] K. Brechtelsbauer and D. Malz, Quantum simulation with fully coherent dipole-dipole interactions mediated by three-dimensional subwavelength atomic arrays, Phys. Rev. A **104**, 013701 (2021).
[48] D. Fernández-Fernández and A. González-Tudela, Tunable directional emission and collective dissipation with quantum metasurfaces, Phys. Rev. Lett. **128**, 113601 (2022).
[49] S. Panyella Pedersen, L. Zhang, and T. Pohl, Quantum nonlinear metasurfaces from dual arrays of ultracold atoms, arXiv:2201.06544.
[50] R. Bekenstein, I. Pikovski, H. Pichler, E. Shahmoon, S. Yelin, and M. Lukin, Quantum metasurfaces with atom arrays, Nat. Phys. **16**, 676 (2020).
[51] Z.-Y. Wei, D. Malz, A. González-Tudela, and J. I. Cirac, Generation of photonic matrix product states with Rydberg atomic arrays, Phys. Rev. Res. **3**, 023021 (2021).
[52] M. Moreno-Cardoner, D. Goncalves, and D. E. Chang, Quantum nonlinear optics based on two-dimensional Rydberg atom arrays, Phys. Rev. Lett. **127**, 263602 (2021).
[53] L. Zhang, V. Walther, K. Mølmer, and T. Pohl, Quantum **6**, 674 (2022).
[54] K. Srakaew, P. Weckesser, S. Hollerith, D. Wei, D. Adler, I. Bloch, and J. Zeiher, A subwavelength atomic array switched by a single Rydberg atom, arXiv:2207.09383.
[55] Y. Solomons and E. Shahmoon, Multichannel waveguide QED with atomic arrays in free space, Phys. Rev. A **107**, 033709 (2023).
[56] D. Barredo, S. de Léséleuc, V. Lienhard, T. Lahaye, and A. Browaeys, An atom-by-atom assembler of defect-free arbitrary two-dimensional atomic arrays, Science **354**, 1021 (2016).
[57] M. Endres, H. Bernien, A. Keesling, Harry Levine, E. R. Anschuetz, A. Krajenbrink, C. Senko, V. Vuletic, M. Greiner, and M. D. Lukin, Atom-by-atom assembly of defect-free one-dimensional cold atom arrays, Science **354**, 1024 (2016).
[58] P. Lodahl, S. Mahmoodian, and S. Stobbe, Interfacing single photons and single quantum dots with photonic nanostructures, Rev. Mod. Phys. **87**, 347 (2015).
[59] D. E. Chang, J. S. Douglas, A. González-Tudela, C. L. Hung, and H. J. Kimble, Rev. Mod. Phys. **90**, 031002 (2018).
[60] M. D. Lukin, M. Fleischhauer, R. Cote, L. M. Duan, D. Jaksch, J. I. Cirac, and P. Zoller, Dipole blockade and quantum information processing in mesoscopic atomic ensembles, Phys. Rev. Lett. **87**, 037901 (2001).
[61] O. Firstenberg, C. S. Adams, and S. Hofferberth, Nonlinear quantum optics mediated by Rydberg interactions, J. Phys. B: At. Mol. Opt. Phys. **49**, 152003 (2016).
[62] D. Petrosyan, J. Otterbach, and M. Fleischhauer, Electromagnetically induced transparency with Rydberg atoms, Phys. Rev. Lett. **107**, 213601 (2011).
[63] M. Arcari, I. Söllner, A. Javadi, S. Lindskov Hansen, S. Mahmoodian, J. Liu, H. Thyrrestrup, E. H. Lee, J. D. Song, S. Stobbe, and P. Lodahl, Near-unity coupling efficiency of a quantum emitter to a photonic crystal waveguide, Phys. Rev. Lett. **113**, 093603 (2014).
[64] S. L. Bromley, B. Zhu, M. Bishof, X. Zhang, T. Bothwell, J. Schachenmayer, T. L. Nicholson, R. Kaiser, S. F. Yelin, M. D. Lukin, A. M. Rey, and J. Ye, Collective atomic scattering and motional effects in a dense coherent medium, Nat. Commun. **7**, 11039 (2016).
[65] Y. Solomons, I. Shani, O. Firstenerg, N. Davidson, and E. Shahmoon, Coupling light to an atomic tweezer array in a cavity, arXiv:2312.11104.
[66] S. Siva, Numerical propagation of $u(\mathbf{r}_\perp)$ is performed via Fresnel diffraction.
[67] E. Shahmoon and G. Kurizki, Nonradiative interaction and entanglement between distant atoms, Phys. Rev. A **87**, 033831 (2013).
[68] A. González-Tudela, D. Martin-Cano, E. Moreno, L. Martin-Moreno, C. Tejedor, and F. J. Garcia-Vidal, Entanglement of two qubits mediated by one-dimensional plasmonic waveguides, Phys. Rev. Lett. **106**, 020501 (2011).

[69] L. D. Landau and E. M. Lifshitz, *Statistical Physics, Part 1* (Pergamon Press, New York, 1980), 3rd ed.

[70] J. Hu, W. Chen, Z. Vendeiro, H. Zhang, and V. Vuletić, Entangled collective-spin states of atomic ensembles under nonuniform atom-light interaction, Phys. Rev. A **92**, 063816 (2015).

[71] D. E. Chang, L. Jiang, A. V. Gorshkov, and H. J. Kimble, Cavity QED with atomic mirrors, New J. Phys. **14**, 063003 (2012).

[72] I. H. Deutsch, R. J. C. Spreeuw, S. L. Rolston, and W. D. Phillips, Photonic band gaps in optical lattices, Phys. Rev. A **52**, 1394 (1995).